

AFRL-SN-RS-TR-2006-15
Final Technical Report
January 2006



STOICHIOMETRIC LITHIUM NIOBATE (SLN) BASED LINEARIZED ELECTRO-OPTIC (EO) MODULATOR

Srico, Inc.

APPROVED FOR PUBLIC RELEASE; DISTRIBUTION UNLIMITED.

**AIR FORCE RESEARCH LABORATORY
SENSORS DIRECTORATE
ROME RESEARCH SITE
ROME, NEW YORK**

STINFO FINAL REPORT

This report has been reviewed by the Air Force Research Laboratory, Information Directorate, Public Affairs Office (IFOIPA) and is releasable to the National Technical Information Service (NTIS). At NTIS it will be releasable to the general public, including foreign nations.

AFRL-SN-RS-TR-2006-15 has been reviewed and is approved for publication

APPROVED: /s/

BRIAN F. MCKEON
Project Engineer

FOR THE DIRECTOR: /s/

RICHARD G. SHAUGHNESSY
Chief, Rome Operations Office
Sensors Directorate

REPORT DOCUMENTATION PAGE			Form Approved OMB No. 074-0188	
Public reporting burden for this collection of information is estimated to average 1 hour per response, including the time for reviewing instructions, searching existing data sources, gathering and maintaining the data needed, and completing and reviewing this collection of information. Send comments regarding this burden estimate or any other aspect of this collection of information, including suggestions for reducing this burden to Washington Headquarters Services, Directorate for Information Operations and Reports, 1215 Jefferson Davis Highway, Suite 1204, Arlington, VA 22202-4302, and to the Office of Management and Budget, Paperwork Reduction Project (0704-0188), Washington, DC 20503				
1. AGENCY USE ONLY (Leave blank)	2. REPORT DATE JANUARY 2006	3. REPORT TYPE AND DATES COVERED Final May 03 – Sep 05		
4. TITLE AND SUBTITLE STOICHIOMETRIC LITHIUM NIOBATE (SLN) BASED LINEARIZED ELECTRO-OPTIC (EO) MODULATOR		5. FUNDING NUMBERS C - F30602-03-C-0103 PE - 62204F PR - 517D TA - SN WU - 01		
6. AUTHOR(S) Dr Stuart Kingsley, Dr Sri Sriram				
7. PERFORMING ORGANIZATION NAME(S) AND ADDRESS(ES) Srico, Inc. 2724 Sawbury Boulevard Columbus Ohio 43235-4579		8. PERFORMING ORGANIZATION REPORT NUMBER N/A		
9. SPONSORING / MONITORING AGENCY NAME(S) AND ADDRESS(ES) Air Force Research Laboratory/SNDP 26 Electronic Parkway Rome New York 13441-4514		10. SPONSORING / MONITORING AGENCY REPORT NUMBER AFRL-SN-RS-TR-2006-15		
11. SUPPLEMENTARY NOTES AFRL Project Engineer: Brian F. McKeon/SNDP/(315) 330-7348 Brian.McKeon@rl.af.mil				
12a. DISTRIBUTION / AVAILABILITY STATEMENT APPROVED FOR PUBLIC RELEASE; DISTRIBUTION UNLIMITED.			12b. DISTRIBUTION CODE	
13. ABSTRACT (Maximum 200 Words) Optical modulators with linearized response functions have been investigated for many years, due to their important applications in analog and RF communications and data transfer links. In particular, a linearized response function offers higher dynamic range because of lower harmonic and intermodulation distortions. Another advantage of a linearized response function is an enhanced tolerance to bias point drift. In evaluating the merit of a linearized design from a systems application perspective, the slope efficiency, defined as the change in intensity per unit change in modulator drive voltage at the operating point, is an important figure of merit. Srico addressed the development of variable coupling in directional coupler modulator devices to improve linearity of the response function. Devices were fabricated and tested in congruent and stoichiometric lithium niobate substrates. Tests on prototype devices showed spurious free dynamic range greater than MZI modulators.				
14. SUBJECT TERMS electro-optic modulator, linearization, directional coupler, variable coupling, optical waveguide, Mach-Zehnder, photonic link, lithium niobate, stoichiometric lithium niobate, spur free dynamic range			15. NUMBER OF PAGES 44	
			16. PRICE CODE	
17. SECURITY CLASSIFICATION OF REPORT UNCLASSIFIED	18. SECURITY CLASSIFICATION OF THIS PAGE UNCLASSIFIED	19. SECURITY CLASSIFICATION OF ABSTRACT UNCLASSIFIED	20. LIMITATION OF ABSTRACT UL	

Table of Contents

Introduction.....	1
Design Technique for Variable Coupler Modulators.....	2
Distortion Calculation.....	5
Coupler Designs and Distortions for the Specific Response	6
Device Design and Fabrication	11
Waveguide Substrate.....	11
Waveguide Fabrication in SLN.....	11
Waveguide Characterization	12
Waveguide Insertion Loss Measurements	15
Waveguide Mode Size Measurements	15
BeamProp Simulations	16
Diffusion Model Parameters.....	16
Directional Coupler Simulations	17
Design of Phase Shifter for the Linearized Coupler	19
Characterization of the PE Phase Shifter.....	20
Photomask Design	21
PSW Structures.....	21
Mask Summary.....	21
Device Fabrication	22
Test Results	23
Device Test Results at Audio Frequency	23
Mach-Zehnder Modulators.....	23
Standard Directional Coupler Modulators (SDCM).....	24
Linearized Directional Coupler Modulators.....	25
PSW Structures.....	27
Spurious Free Dynamic Range (SFDR) Measurements	29
Mach-Zehnder Modulator.....	30
Linearized Directional Coupler Modulator SFDR Measurements	32
Discussion.....	37
References.....	38

Table of Figures

Figure 1. Ideal response function of a linearized optical modulator.....	1
Figure 2. Schematic of the uniform coupling coupler modulator	2
Figure 3. (a) Desired trapezoidal response function; (b) Coupling function for the response.	4
Figure 4. (a) Enlarged view of the trapezoidal response; (b) Distortion calculations.....	5
Figure 5. (a) Coupling Coefficient; (b) Response for the original trapezoidal case.	6
Figure 6. SFDR for (a) IMD2 and IMD3; (b) 2 nd and 3 rd harmonic for trapezoidal response.	6
Figure 7. (a) Coupling coefficient (b) Response for the improved trapezoidal case.	7
Figure 8. SFDR for (a) IMD2 and IMD3; (b) 2 nd and 3 rd harmonic for design of Figure 7.	7
Figure 9. (a) Coupling coefficient (b) Response for design using quadratic arcs.	8
Figure 10. SFDR for (a) IMD2 and IMD3; (b) 2 nd and 3 rd harmonic for design of Figure 9.	8
Figure 11. (a) Coupling coefficient for Pi-phase shift design; (b) Coupler response.	9
Figure 12. SFDR for (a) IMD2 and IMD3; (b) 2 nd and 3 rd harmonic Pi-phase shift design.	9
Figure 13. Simulations comparing standard directional coupler to linearized Pi-phase shift design	10
Figure 14. Change in o- and e-indices calculated for Ti diffused waveguide in CLN.....	13
Figure 15. Micrograph of TM mode for 6 micron waveguide.....	14
Figure 16. Sample screenshot showing a measured mode	15
Figure 17. Simulated mode that matches the experimental Ti:SLN mode	17
Figure 18. Simulated coupling length dependence on the waveguide gap	17
Figure 19. Plots of coupling length vs. various perturbed fabrication parameters.....	18
Figure 20. Schematic of MZI and SDCM devices.....	22
Figure 21. Schematic of a LDCM device	22
Figure 22. MZI Modulator response for device 3Z2c4.MZ2 fabricated in CLN.....	23
Figure 23. MZI Modulator response for device 2Z2c4.MZ1 fabricated in SLN	23
Figure 24. Standard Coupler response in the Bar state	24
Figure 25. Standard Coupler response in the Cross state.....	24
Figure 26. SLN Linearized Coupler response in the Bar state.....	25
Figure 27. SLN Linearized Coupler response in the Cross state	25
Figure 28. Theoretical MZI response superimposed on a typical LDCM characteristic	26
Figure 29. Input PSW structure.....	27
Figure 30. Output PSW structure.....	27
Figure 31. Test system for the measurement of SFDR	29
Figure 32. SFDR plot for a MZI modulator for received optical power of 0 dBm.....	31
Figure 33. SFDR plot for a MZI for extrapolated mean received optical power of +10 dBm.....	31
Figure 34. Characterization of New Focus 1617 receiver as a function of mean received optical power ..	33
Figure 35. Intermodulation frequency spectrum for LDCM device	34
Figure 36. SFDR plot for a bias voltage of +1.74 V and received power of -2 dBm	34
Figure 37. SFDR at a bias voltage of +1.74 V extrapolated to a received power of +10 dBm.....	35
Figure 38. SFDR plot for a bias voltage of +1.54 V and a received power of -1 dBm.....	36
Figure 39. SFDR at a bias voltage of +1.54 V extrapolated to a received power of +10 dBm.....	37

List of Tables

Table 1. Results of prism coupling measurements on Ti slab regions	13
Table 2. Mode size at 60% max intensity calculated using a fit to a Gaussian profile	14
Table 3. Horizontal and vertical FWHM intensity of Ti channels.....	16
Table 4. Photomask summary	21
Table 5. Optical transmission loss for a PSW structure.....	28
Table 6. Mode size for a 7 micron PSW waveguide.....	28

INTRODUCTION

Optical modulators with linearized response functions have been investigated for many years^{1,2} due to their important applications in analog and RF communications and data transfer links. In particular, a linearized response function offers higher dynamic range because of lower harmonic and intermodulation distortions. Another advantage of a linearized response function is an enhanced tolerance to bias point drift. In evaluating the merit of a linearized design from a systems application perspective, the slope efficiency, defined as the change in intensity per unit change in modulator drive voltage at the operating point, is an important figure of merit. This quantity depends not only on the shape of the response function, but also scales with the insertion loss, which acts as an overall multiplicative factor.

Recently, developments in linearized directional coupler modulator design have yielded encouraging results that promise high linearity and high slope efficiency for analog and RF communications applications.³ These designs rely on a coupling coefficient which varies along the length of the coupler. These designs are synthesized based on the small-coupling limit, where a Fourier conjugate relationship exists between the coupling and response functions. Various synthesis techniques have been developed⁴ which first apply an inverse Fourier transform to the desired response function to determine an approximate coupling function and then iterate the design until the desired response function is achieved. In particular, the ideal response function has very linear, very steep transition, as shown in Figure 1.

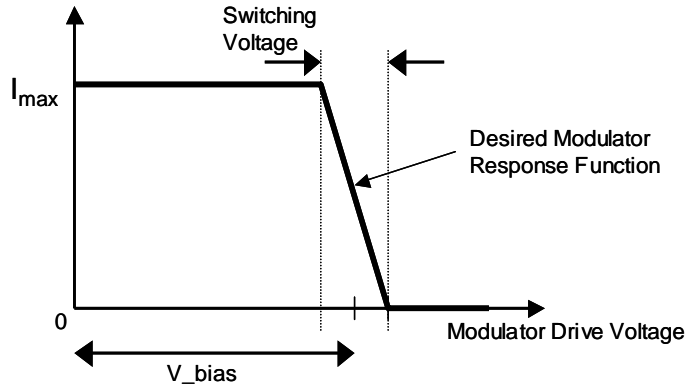


Figure 1. Ideal response function of a linearized optical modulator

DESIGN TECHNIQUE FOR VARIABLE COUPLER MODULATORS

Recent theoretical work has shown that in grating assisted contra-directional couplers and filters, the grating design may be synthesized by the inverse scattering technique based on the theory of Gel'fand, Levitan, and Marchenko (GLM)⁵. This technique requires that the response function be expressed as a rational polynomial, and has resulted in designs based on the usual Butterworth, Chebyshev polynomials. Further work by Peral⁶ has shown that the response functions that cannot be represented by rational polynomials may also be synthesized with this technique using the inverse Fourier transform method, to obtain the first guess, and subsequently an iterative method is used to obtain the required grating design. The lack of symmetry of these designs results in the introduction of chirp and therefore this technique was not considered further.

An alternative is the inverse Fourier transform method discussed in Tamir's book⁷, and assumes that the coupling is very small, and thus the method is at best approximate. A detailed design has been discussed by Winick⁸ for a grating coupled filter based on the Fourier transform method. For the co-directional coupler with constant coupling, the coupling function is a rectangular pulse, and the spatial Fourier transform is the sinc function, which is the response of the output field. Thus, the intensity response has the sinc^2 form, and the coupling and response functions are related through the Fourier and inverse Fourier transform. Thus, if the desired intensity response function is known, the coupling function may be derived from the inverse Fourier transform. Since this Fourier technique is approximate, a Newton's method modification has been suggested, which obtains the coupling function from the desired response function without the small coupling limitation.³ Using these design methods, semiconductor coupler modulators built have shown that the variable coupling design works very well.^{4,9,10,11,12,13,14,15,16}

The schematic diagram for the coupler is shown in Figure 2, with the two guides in close proximity to each other, with the input to guide 1 given as $R(0)$, and the input to the second guide $S(0)$. When the signal is placed on the first guide of the uniform coupler modulator, both the even and odd supermodes of this coupler are excited, with the modes adding constructively in this first guide and destructively in the second guide. The signal which is now the superposition of the two modes travels down the coupler with the odd mode velocity being slightly higher. A specific distance later the phases of the odd and even modes are interchanged because of the difference in velocities, so that the modes add constructively in the second guide, but destructively in the first, in effect causing a transfer of power from guide one to guide two.

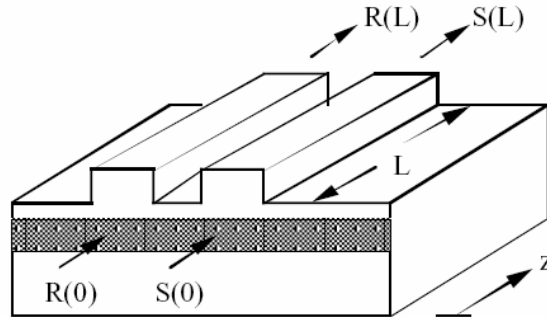


Figure 2. Schematic of the uniform coupling coupler modulator

The coupled mode equations for the directional coupler are given by:

$$\frac{\partial R}{\partial z} = j\delta R - j\kappa(z)S e^{-j\phi(z)} \quad (1)$$

$$\frac{\partial S}{\partial z} = -j\delta S - j\kappa(z)R e^{j\phi(z)} \quad (2)$$

where R and S are the complex amplitude fields in the guides as a function of z , spatial position along the coupler, $\kappa(z)$ is the coupling coefficient which is a slowly varying function of z , $\Delta\beta$ is the difference in the propagation constants of the two guides uncoupled, $\delta = \Delta\beta/2$, and

$$\phi(z) = \int_0^z [\Delta\beta(z') - \Delta\beta(0)] dz' \quad (3)$$

In the directional coupler modulator, the guides are made identical to each other, so that $\Delta\beta$ is zero in the unbiased condition, and the application of bias makes $\Delta\beta$ nonzero, and hence δ is also nonzero.

The solution to these equations for an uniform coupler of length L , with initial conditions of $R(0) = 1$ and $S(0) = 0$, is given by:

$$R(z) = \cos(z\sqrt{\kappa^2 + \delta^2}) + j\delta \frac{\sin(z\sqrt{\kappa^2 + \delta^2})}{\sqrt{\kappa^2 + \delta^2}} \quad (4)$$

$$S(z) = -j\kappa \frac{\sin(z\sqrt{\kappa^2 + \delta^2})}{\sqrt{\kappa^2 + \delta^2}} \quad (5)$$

The amplitude response of the uniform coupler modulator is given by:

$$\eta \equiv |S(z)|_{R(0)=1, S(0)=0}^2 = \frac{\sin^2\left(\kappa z \sqrt{1 + (\delta/\kappa)^2}\right)}{1 + (\delta/\kappa)^2} \quad (6)$$

Define the coupling length L_c as the distance when all the power in the first guide of the uniform coupler is transferred to the second, or $|S|=1$. In the case when there is no bias which implies $\delta = 0$, then from equation (5), $L = L_c = \pi/(2\kappa)$. For the case when bias is applied so that δ is not zero, for $L = L_c$, it follows that $\delta_{switch}/\kappa = \sqrt{3}$ or $\delta_{switch}L_c = \sqrt{3}\pi/2$. Also when the two guides are biased so as to have different effective indices, then by definition

$$\delta = \Delta\beta/2 = (n_{guide1} - n_{guide2})\pi/\lambda_0 = \Delta n_{guide}\pi/\lambda_0 \quad (7)$$

The difference in the guide effective indices due to bias is given by equation (7):

$$\Delta n_{guide} = (n^3 r_{xx} VT)/(2d) \quad (8)$$

where n is the guide mean effective index, r_{xx} is the electro-optic coefficient depending on the direction of the field interacting with the optical mode, V is the voltage applied to the coupler electrodes, d is the distance between the electrodes, and Γ is the overlap integral between the bias electric field and the electric field of the optical mode. Substituting for the δ from equation (7):

$$V_{\text{switch}}L_c = p(\lambda_0 d)/(n^3 r\Gamma) \quad (9)$$

where

$$p = \delta_{\text{switch}}L_c / \pi = \sqrt{3}/2 \quad (10)$$

for push-pull electrode excitation of the uniform coupler.

Using the transformation to the Ricatti equation^{7,4}, it can be shown for very small coupling that S and κ are related through the Fourier transform equation of the form:

$$\kappa(z) \approx \frac{2}{\pi} \int_0^\infty |S(\delta)| \cos(2\delta z) d\delta \quad (11)$$

Thus, if the desired intensity response for the coupler modulator is given by $|S(\delta)|^2$, the first guess with small coupling is obtained from the above equation (11). The coupling function derived from this equation extends to $\pm\infty$, and needs to be truncated symmetrically to prevent chirp being generated. The truncated coupling function will only provide an approximate form of the desired response, and thus needs to be modified to provide a closer agreement. The next step uses the Newton's method,³ with this truncated response as the first guess. The error in the response function is evaluated, the appropriate Jacobian is obtained, and by the least squares method, the correction is obtained. Subsequent iterations move the coupling function closer to the desired response function. Figure 3(a) shows the desired response function in the form of a trapezoid, and the iterated response from the modified coupling function, shown in Figure 3(b).

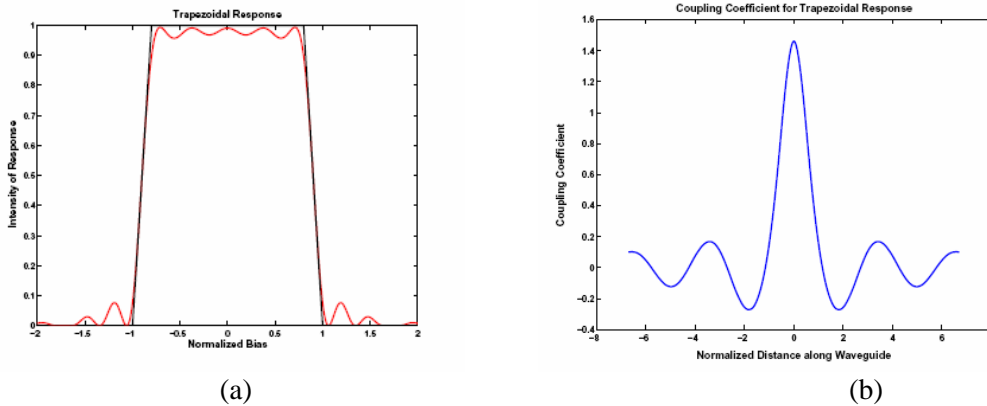


Figure 3. (a) Desired trapezoidal response function; (b) Coupling function for the response.

Distortion Calculation

The usual technique for calculating the distortions in modulators is to express the response function as a polynomial in the applied voltage, and thus for the present case the output signal power is

$$|S|_{out}^2 = a_0 + a_1 V_{appl} + a_2 V_{appl}^2 + a_3 V_{appl}^3 + a_4 V_{appl}^4 + \dots \quad (12)$$

However, expressing the response function in polynomial form results in considerable error and the results are not accurate.

Another method is to superpose two signals at slightly different frequencies, and take the Fourier transform, either in the FFT technique or in the usual integral form. However, it is necessary that the periodicity is not violated by taking too small a sequence, and this also results in inaccuracies due to the large number of points required.

The most accurate method is to use the 2D FFT technique in which the two dimensions correspond to the time periods of the two tones passed through the modulator simultaneously. Matlab and other programs have this as a standard function, but it is also possible to program it to work with the single FFT code. Figure 4(a) shows the trapezoidal response function, with the enlarged section of the response curve. Figure 4(b) shows the harmonics, which lead to $2f$ and $3f$ results with different drive levels. For the two tones case, the intermodulation distortion is created. The second order intermodulation distortion (IMD2) and third order intermodulation distortion (IMD3), which leads to $2f_1 - f_2$ and $2f_2 - f_1$, are usually used to measure the linearity of the devices. Drawing the noise floor provides the spur free dynamic range (SFDR), which is the vertical distance from the intersection of the noise floor of the IMD3 line to the fundamental power at that point.

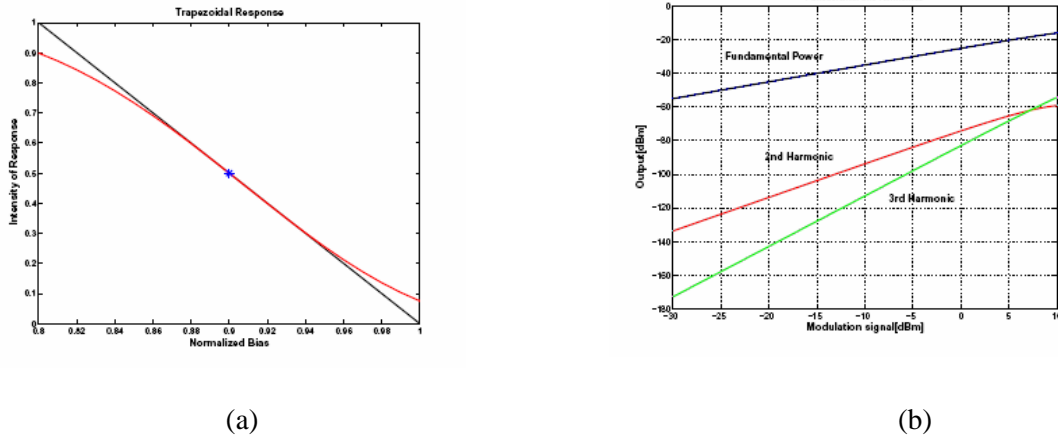


Figure 4. (a) Enlarged view of the trapezoidal response; (b) Distortion calculations.

Coupler Designs and Distortions for the Specific Response

Trapezoidal Response

The curve in Figure 5(a), is the coupling function for trapezoidal response. In Figure 5(b), dash-line is the desired response and solid line is the obtained response from the coupling function in Figure 5(a) by the iterative method.

Shown in Figure 6(a) are the IMD2 and IMD3 calculated with $R=0.9$ A/W, $V_{SW}=2.0$ V (0.8 to 1 in the normalized response in Figure 3(b)), noise floor = -160 dBm. From Figure 6(a) and (b), the third harmonic is a little higher than IMD3, and the second harmonic and IMD2 have the same values; but the second harmonic is higher than IMD2 at the peak value.

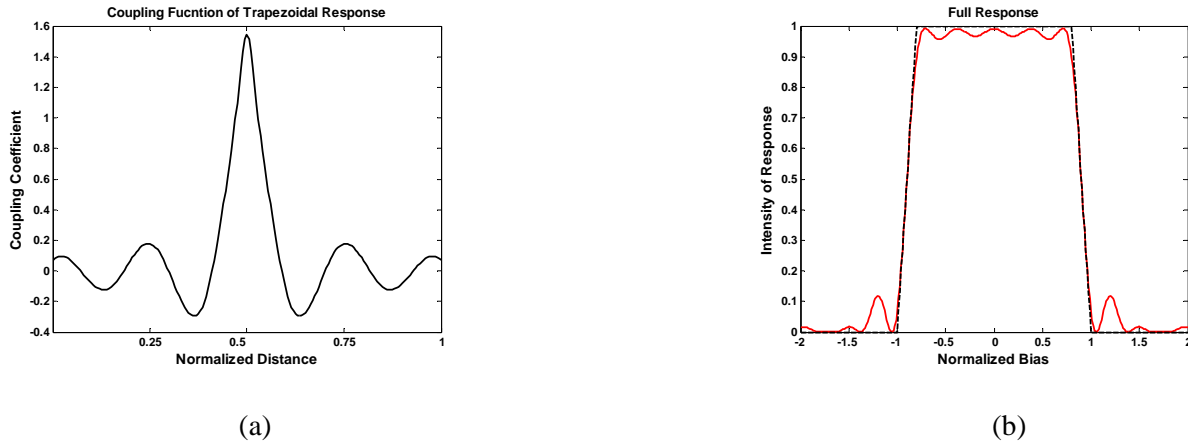


Figure 5. (a) Coupling Coefficient; (b) Response for the original trapezoidal case.

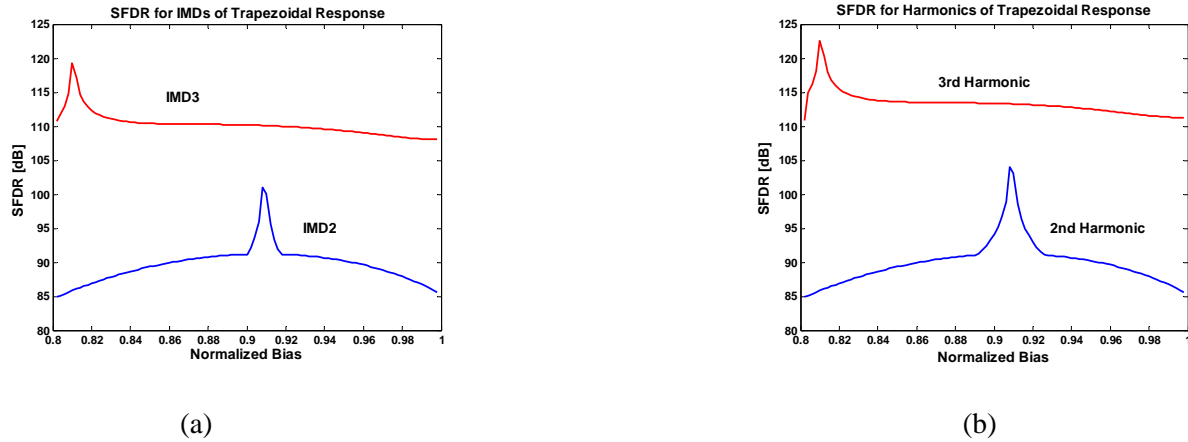


Figure 6. SFDR for (a) IMD2 and IMD3; (b) 2nd and 3rd harmonic for trapezoidal response.

Modified Trapezoidal Response

Trapezoidal response with ideal response having arcs of circles as curved regions, in Figure 7, has better IMD2 and IMD3 results as shown in Figure 8. These were calculated with $R=0.9$ A/W, $V_{SW}=2.0$ V (0.3 to 1.5 in the normalized response), optical input power=10 mW, noise floor set at -160 dBm. The second harmonic and the third harmonic are shown in Figure 8(b). The third harmonic is a little higher than IMD3, and the second harmonic and IMD2 have the same values; but the second harmonic is a little higher than IMD2 at the peak value.

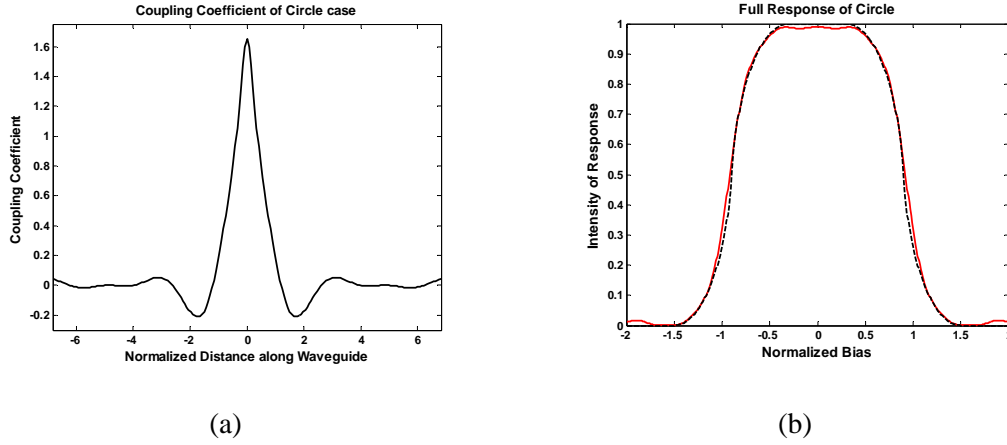


Figure 7. (a) Coupling coefficient (b) Response for the improved trapezoidal case.

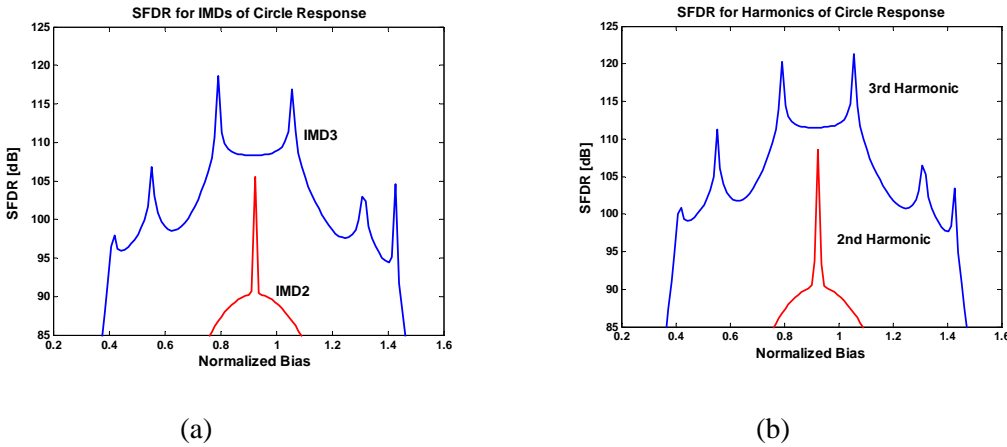


Figure 8. SFDR for (a) IMD2 and IMD3; (b) 2nd and 3rd harmonic for design of Figure 7.

Another design which uses a straight line with a slightly lower slope and quadratic arcs in beginning and end regions of the switching sections for the trapezoidal response is shown in Figure 9. IMD3 and IMD2 shown in Figure 10(a) are found to be better than those of original trapezoidal case.

These were calculated with $R=0.9$ A/W, $V_{sw}=2.0$ V (0.3 to 1.5 in the normalized response), optical input power=10 mW, noise floor set at -160 dBm. The second harmonic and the third harmonic are shown in Figure 10(b). The third harmonic is a little higher than IMD3 and the second harmonic and IMD2 have the same value, but the second harmonic is a little higher than IMD2 at the peak value.

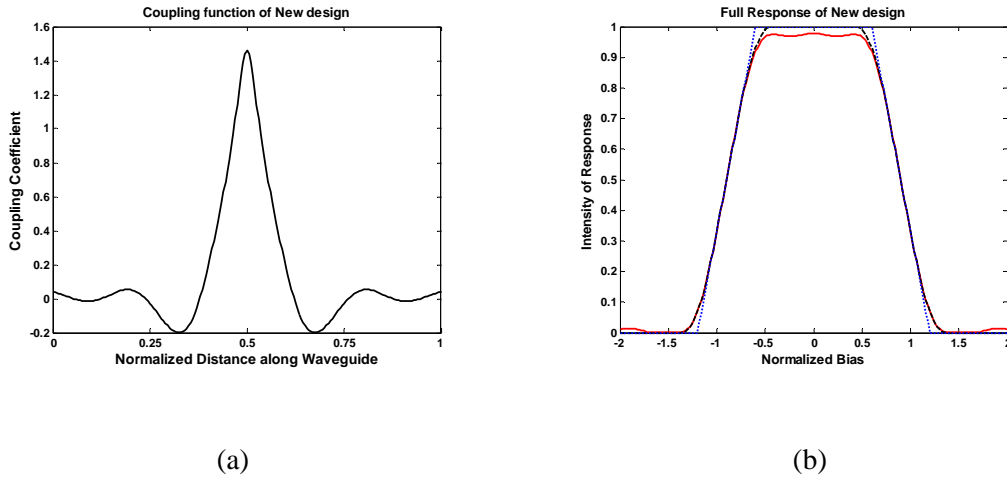


Figure 9. (a) Coupling coefficient (b) Response for design using quadratic arcs.

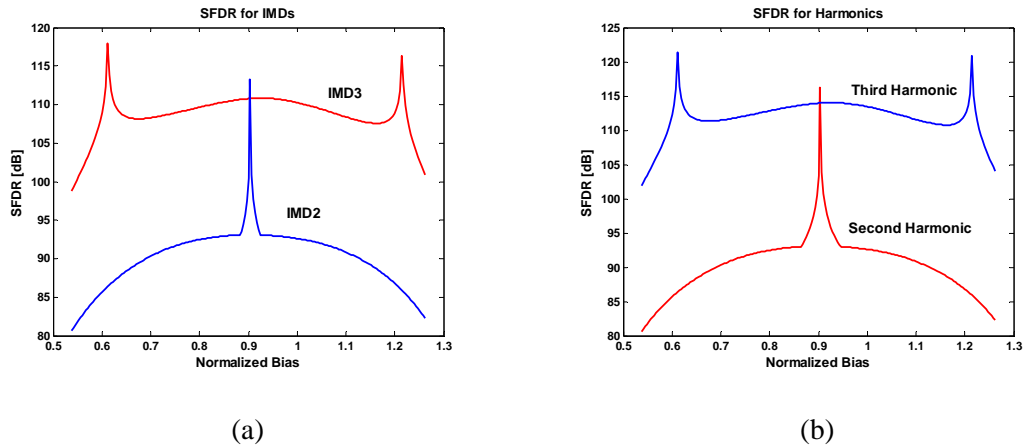


Figure 10. SFDR for (a) IMD2 and IMD3; (b) 2nd and 3rd harmonic for design of Figure 9.

Uniform Coupling with Phase Change Design (Pi-Phase Shift Design)

The directional coupler design which has constant coupling coefficient over the entire device length with four phase shifts is shown in Figure 11(a) with the locations of the phase shifts. In this design the magnitude of the coupling coefficient is constant over the length of the coupling region, and phase control is limited to four identical phase shifters, each providing a 180° phase shift and thus reversing the sign of the coupling coefficient. We refer to this as the “Pi Phase Shift” design.

The response is shown in Figure 11(b). The SFDR for IMDs and Harmonics from this response has greater values than 120dB, shown in Figure 12. These were calculated with $R=0.9$ A/W, $V_{SW}=2.0$ V (0.3 to 1.5 in the normalized response), optical input power=10 mW, noise floor set at -160 dBm. The third harmonic is a little higher than IMD3 and the second harmonic and IMD2 have the same values, but the second harmonic is higher than IMD2 at the peak value.

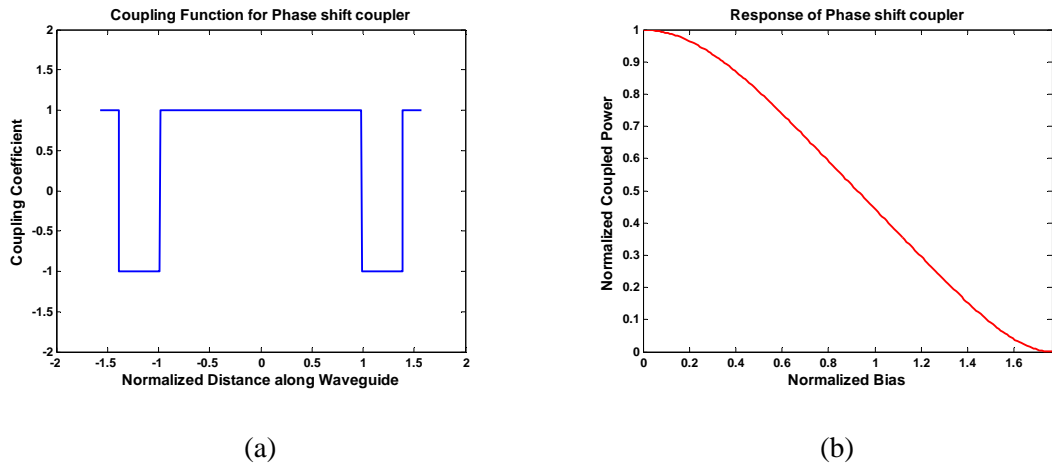


Figure 11. (a) Coupling coefficient for Pi-phase shift design; (b) Coupler response.

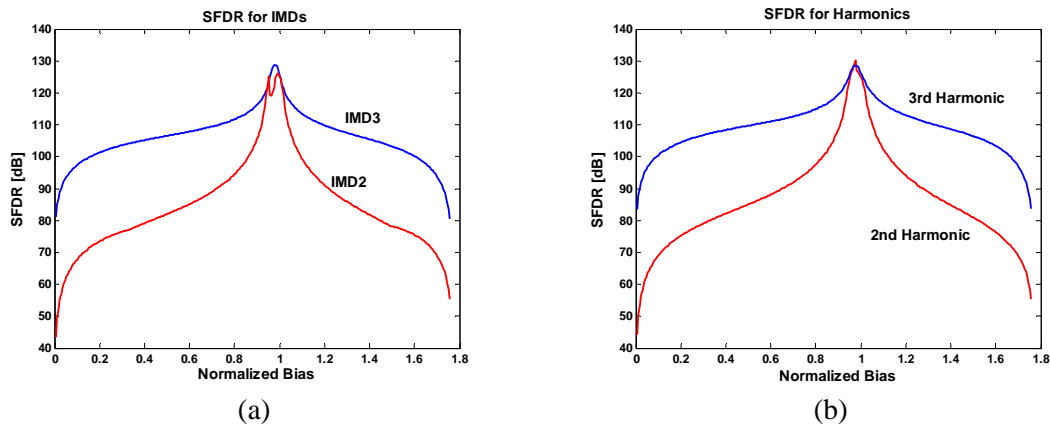


Figure 12. SFDR for (a) IMD2 and IMD3; (b) 2nd and 3rd harmonic Pi-phase shift design.

The operation of the Pi phase shift design is modeled using transfer matrices from coupled mode theory. Figure 13 illustrates the behavior of the Pi phase shift design (lower graphs) compared to the standard directional coupler (upper graphs). Shown on the left is the evolution of the optical fields in the two

waveguides as a function of distance along the coupler. Multiple curves are shown corresponding to increasing drive voltage. In the standard directional coupler, no applied voltage results in a complete power exchange between the two waveguides. Increasing the drive voltage both shortens the period and lowers the magnitude of the exchange. At the switching voltage (the largest voltage pictured), the input light returns to the original waveguide by the end of the device. At the right is shown the corresponding transfer function.

In contrast, the Pi phase shift design (lower graphs) shows the effect of the 180° phase shifters on the power transfer. Again, multiple curves are shown corresponding to increasing drive voltage. In each case, the evolution follows a fixed periodicity (due to fixed magnitude coupling coefficient) punctuated by abrupt reversals at the locations of the phase shifters. At right is the corresponding response function plotted with drive voltages corresponding to the individual curves at the left. The linearization of the response function is evident even when plotted with just a few data points, as shown.

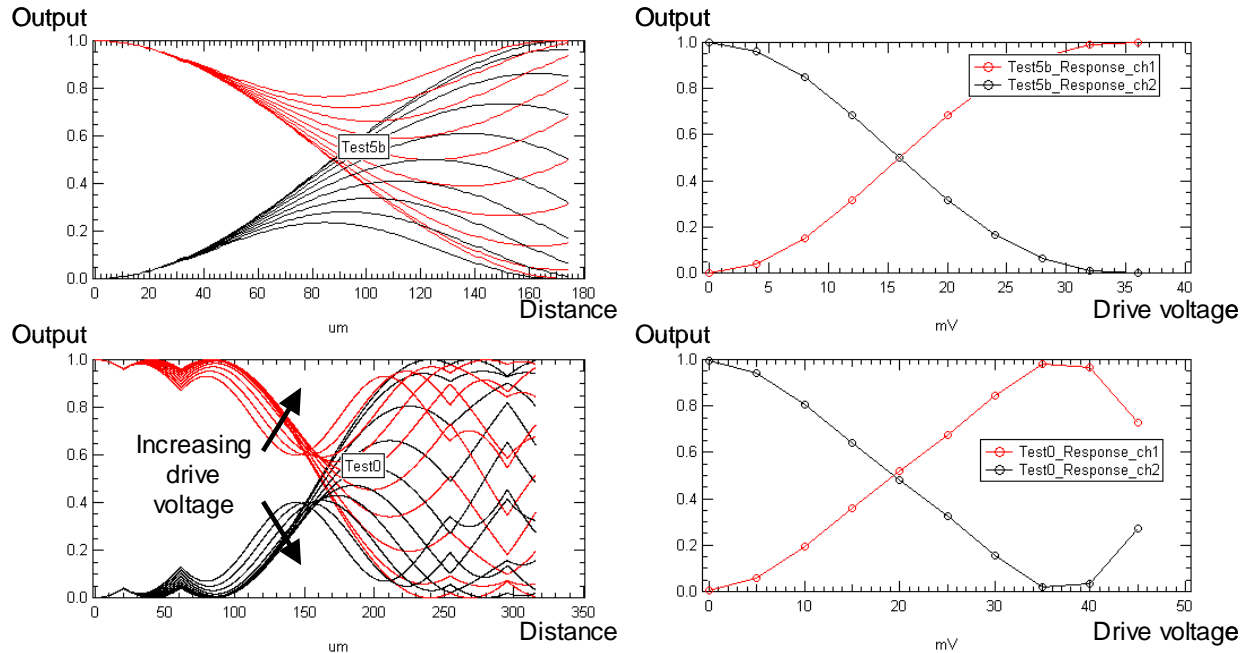


Figure 13. Simulations comparing standard directional coupler to linearized Pi-phase shift design

DEVICE DESIGN AND FABRICATION

Waveguide Substrate

Achieving the goal of state-of-the-art modulator performance requires not only innovative optical circuit designs, but innovative materials systems and processing techniques. Today lithium niobate (LN) is the preferred substrate for electro-optic devices such as high-speed modulators and switches. This remarkable material is expected to remain the preferred substrate for these applications, while expanding into a variety of new application areas such as nonlinear optical generation, advanced modulation formats, optical packet switching, wavelength conversion, and holographic storage. Optoelectronic integration with high-speed electronics using GaN epitaxial layers on LN is an important example of recent advances in materials and devices that promise continued dominance of LN in a variety of applications. The recent availability of stoichiometric lithium niobate (SLN), with a host of enhanced properties, promises somewhat of a renaissance in the world of LN applications. Stoichiometric lithium niobate (SLN) has better nonlinear, electro-optic, and ferroelectric properties than the commonly produced congruent lithium niobate (CLN). In this report we outline our current research program that is implementing new linearized directional coupler designs on the new material SLN.

Lithium niobate is normally produced by pulling crystals from a melt with a Nb to Li mole ratio of 51.5% to 48.5%. This composition, called the congruent composition, has been preferred because this is the composition where the solid coexists with a single phase melt. Congruent lithium niobate (CLN) is thus the substrate used for all commercially available optical waveguide products today. The off-stoichiometric composition, while convenient for crystal growth, has several well-documented disadvantages relative to SLN. The advantages of SLN over CLN include:¹⁷

- Increased nonlinear coefficient (44.3 pm/V vs. 34.1 pm/V), which translates directly into an increased electrooptic coefficient (38.3 pm/V vs. 31.5 pm/V)
- Better high optical power handling characteristics¹⁸ (lower Mg doping percentage, 1% vs. 5% for 1 MW/cm² power handling capability at 532nm)
- Enhanced ferroelectric properties (higher ferroelectric Curie temperature, and lower coercive field for domain inversion)
- Greater optical transparency range (UV band edge at 305 nm vs. 325 nm)

These enhanced electro-optic and ferroelectric properties arise naturally from the lower intrinsic defect density in the lattice at the stoichiometric composition. In the congruent crystal structure, excess Nb ions occupy Li sites, with charge compensation achieved either by Nb or Li vacancies, or both¹⁹.

Waveguide Fabrication in SLN

Diffused optical waveguide production in SLN is a new area, with very little reported in the current literature. Yuki et al.²⁰ provided the first report of Ti waveguides produced in SLN. They report on production of slab waveguides at temperatures ranging from 1000°C to 1060°C, and with diffusion times ranging from 6 to 24 hours. Prism coupling measurements in these slab regions, along with the assumption of a Gaussian refractive index profile, yielded diffusion coefficient values. They found that the diffusion coefficients of SLN are smaller than in CLN, and, by diffusing into both x-cut and z-cut samples, found that there is less anisotropy to the diffusion coefficients. They also found that the same Ti concentration in SLN yields a higher index change than in CLN. Nakajima et. al.²¹ find that longer diffusion times are required for Ti waveguide production relative to standard SLN recipes. They also report a more nearly isotropic diffusion, in contrast to CLN where the diffusion coefficient in the z direction is known to be larger than that in the x (or y) direction. Caccavale et. al.²² report similar findings in a study of Ti diffused slab waveguides probed by secondary ion mass spectroscopy (SIMS). The

smaller diffusion coefficients found in these studies are in agreement with our results on Ti diffused waveguide production.

Our Ti diffused channel waveguide production recipe was based on the results of mode field calculations and the diffusion coefficients reported by Yuki et al. We diffused 90 nm thick Ti into z-cut SLN for 22 h at 1050°C. The Ti patterning provided both a large slab (planar) waveguide region and a series of y-propagating waveguides with widths ranging from 5.0 μm to 10.0 μm in 0.5 μm increments.

We find that Ti waveguide production on SLN requires longer processing times due to slower diffusion of Ti into the crystal. We find that single mode Ti waveguides can be fabricated with mode size similar to those fabricated in CLN for commercial modulators. The loss of the waveguides was found to be high, on the order of 1 dB/mm, likely due to scattering losses at the rough surface where a thick (~ 200 nm) Ti oxide was left at the surface after Ti indiffusion. The waveguide losses were reduced to acceptable values (~ 0.1 dB/cm) through the process of surface planarization. This is suitable for device fabrication. Fabrication of proton exchanged slab and channel waveguides in SLN is also an active area of research, and our results indicate increased diffusion times for waveguide production relative to CLN.

Waveguide Characterization

The first step in characterizing the Ti diffusion process was to measure the mode spectrum in the planar Ti slab waveguides using prism coupling. Our apparatus consisted of a Rutile (TiO_2) prism, fiber-coupled laser sources at 635, 980, 1310, and 1550 nm, precision rotation stage to accurately measure incidence angles, and a detector to record reflected intensity as a function of incidence angle. As the incidence angle reaches the angle for total internal reflection in the substrate, the intensity of the reflected light will show a sharp increase. Increasing the angle further will show one or more narrow minima, each with a corresponding “flash” of light in the substrate, as the tangential component of the incident wave vector is phase matched to waveguide modes. The measurements thus yielded the bulk index of the substrate, the number of guiding modes and their effective indices. We fitted the resulting mode spectrum to that from a step-index slab using the slab refractive index and thickness as unknown fitting parameters.

Table 1 shows results of the mode spectrum measurements and fitted step-index slab parameters. Also shown for comparison is the CLN index calculated from an accepted Sellmeier form. We used 635 nm and 1550 nm wavelengths, each with both TE and TM incident polarized light. The relevant case for device applications is 1550 nm TM polarized light, because TM light in z-cut substrate sees the extraordinary crystal index. As expected, 635 nm light gave more modes in proportion to the shorter wavelength relative to 1550 nm. The 635 nm measurements thus gave a better step-index slab fit. We emphasize that the step-index slab fit is not expected to provide an accurate characterization of the index depth profile, but rather is used as a convenient way to compare results from different samples or at different polarizations. We see the step-index fitted index delta is larger for TM than for TE. This is consistent with the observed behavior in standard CLN. A standard diffusion model²³ gives the change in refractive index as a power law function of Ti ion concentration. The exponent is 1.0 for the extraordinary index, but only 0.65 for ordinary index. Thus, as shown in Figure 14, for high enough Ti concentration the extraordinary index delta becomes much larger than the ordinary index delta. A comparison with the fitted index delta values shows reasonable agreement with this result, indicating a Ti concentration in the range of 0.020 – 0.040.

	Wavelength	Polarization	# Modes	Sellmeier Index	Measured Substrate Index	Best Fit Step Index	Delta Index	Best Fit Step Height
Ti:+zSLN	635	TM	4	2.2022	2.1923	2.2213	0.0290	3.1
	635	TE	2	2.2858	2.2905	2.2973	0.0068	3.3
	1550	TM	2	2.1381	2.1278	2.1514	0.0236	5
	1550	TE	1	2.2112	2.2130	NA	NA	NA
Ti:-zSLN	635	TM	4	2.2022	2.1882	2.2160	0.0278	3.2
	635	TE	2	2.2858	2.2860	2.2978	0.0118	2.4
	1550	TM	2	2.1381	2.1275	2.1528	0.0253	4.1
	1550	TE	1	2.2112	2.2120	NA	NA	NA

Table 1. Results of prism coupling measurements on Ti slab regions

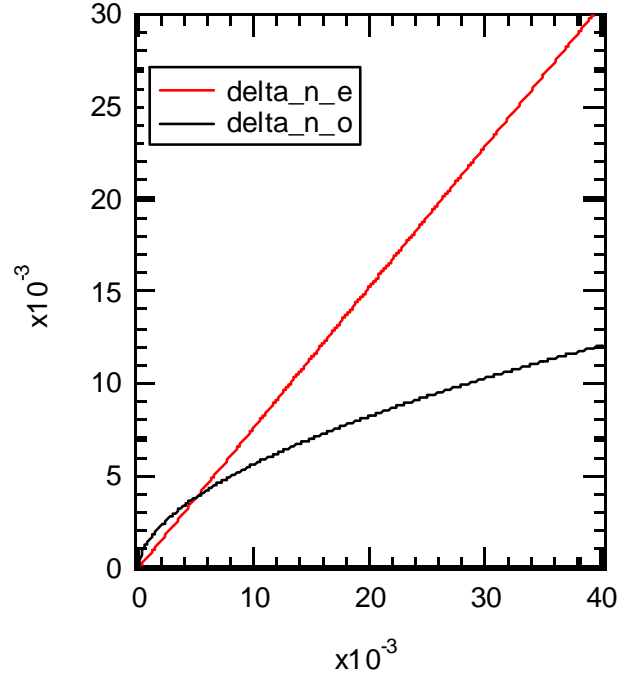


Figure 14. Change in o- and e-indices calculated for Ti diffused waveguide in CLN

Channel waveguides of widths 5.0 – 10.0 μm were characterized by making mode field measurements using the near-field imaging technique. The near-field technique uses a microscope objective lens to image the endface of the waveguide on the focal plane of the IR camera. With proper radiometric calibration (camera gamma = 0.7) and use of neutral density filters calibrated at 1550 nm, Gaussian beam size and beam power can be measured using this system. Our apparatus included a 1550 nm DFB laser, 20x objective lens, an ElectroPhysics 7290A IR camera, and Photon Inc. Model 2350 Laser Beam Profiler, including frame capture board and analysis software.

The optical chip was prepared by dicing and polishing the chip endfaces where the waveguides terminate. The PM fiber pigtail of the laser source was terminated in a fiber block that was aligned to the waveguide input using nanopositioning stages. The slow axis of the PM optical fiber was oriented perpendicular to the crystal surface, and the orthogonal polarization was launched into the waveguide by adding a patch cord with a 90° difference between the PM fiber slow axis relative the connector key. The fiber block was

angle polished at 15° and the waveguide chip was angle polished at 10° , yielding low reflection losses while satisfying the ray optics launch condition.

Shown in Figure 15 is a typical near-field image of a single-moded waveguide. Contrary to the result reported in Ref. 20, who report a (desirable) circular mode shape, we observe elliptically shaped modes. Table 2 shows the results of mode field measurements on sample waveguides diffused into the $+z$ surface. The results for the other sample, with waveguides diffused into the $-z$ surface, were very similar. We note that the mode size is typically $5 \times 7 \mu\text{m}$, very similar to the modes formed in CLN using the standard Ti indiffusion recipe described above. The modes are consistently smaller for TM polarized light (the polarization of interest for devices), consistent with the observation above that the TM index delta is larger. The second mode cutoff occurs at about $6.0 - 7.0 \mu\text{m}$ Ti stripe width, similar to the cutoff stripe width for a standard CLN waveguide recipe. These results indicate the recipe for SLN has successfully been adjusted to account for the smaller diffusion constants of SLN and that acceptable size modes are present in the waveguides.

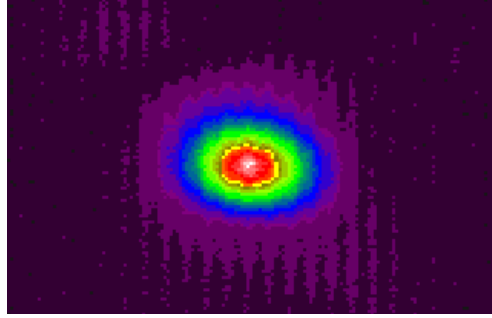


Figure 15. Micrograph of TM mode for 6 micron waveguide

Waveguide Width [μm]	TE Mode Size		Number of Modes	TM Mode Size		Number of Modes
	transverse	normal		transverse	normal	
5.0	7.3	4.8	1	6.4	3.6	1
5.5	7.4	4.4	1	6.4	3.9	1
6.0	9.7	4.7	1	7.3	3.7	1
6.5				7.3	4.8	1
7.0				8.8	4.9	2
7.5	8.5	5.5	2	15.7*	5.5	2
8.0	15.5*	6	2	13.4*	4.7	2

* Gaussian fit to data not valid due to two modes

Table 2. Mode size at 60% max intensity calculated using a fit to a Gaussian profile

Waveguide Insertion Loss Measurements

The slow diffusion of Ti into SLN allows more time for the formation of a thick layer of undiffused deposits, potentially yielding higher insertion loss waveguides than produced in SLN. Indeed, waveguide insertion loss is found to be high, with measured 43 – 45 dB loss in a waveguide of length 40 mm, representing loss of approximately 1 dB/mm. Unfortunately, a comparison with Ref. 20 is not possible, as they do not report the length of the waveguides that show 5dB loss. Since this loss value is too high for commercial applications, the problem was overcome by modifying the waveguide recipe to yield a low loss waveguide.

Waveguide insertion loss was measured using a butt coupled fiber launch of 1550nm light into the waveguide and using a calibrated near-field mode imaging apparatus to measure insertion loss. This apparatus is also used to measure mode field sizes, and consists of fiber pigtailed 1550nm source, sub-micron alignment stages, waveguide launch via carrier (also known as a fiber block), objective lens, various calibrated neutral density (ND) filters, ElectroPhysics 7920 IR camera, and Photon Inc. BeamPro software. Insertion losses were measured using the power measurement capabilities of the camera/software system, in conjunction with various ND filters. The insertion loss measurements using this technique have an experimental error of about ± 1 dB due to the ND filter usage (calibration and Fresnel reflection effects).

We measured insertion losses in three sets of waveguides and found waveguide losses of <1 dB/cm. This loss value is larger than observed for standard Ti:CLN waveguides, however is acceptable for device fabrication. We believe the insertion loss can be reduced further by refining the processing.

Waveguide Mode Size Measurements

Mode field measurements were performed simultaneously with the insertion loss measurements. Figure 16 shows a typical mode. The experimental Ti:SLN mode field measurements are shown in Table 3, quoted as FWHM of the beam intensity. The experimental error is about $\pm 0.5 \mu\text{m}$. We observe mode size on the order of $3 \times 5 \mu\text{m}^2$. It is clear that the errors dominate any trend in mode field size with Ti strip width.

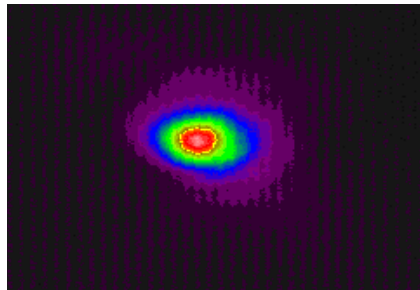


Figure 16. Sample screenshot showing a measured mode

	Unit Cell	Average	
Mode	channel width	height (FWHM)	width (FWHM)
TM	5	3.36	5.43
TM	6	3.14	5.11
TM	7	3.79	6.41
TM	7.5	3.06	5.60
TM	8	3.15	5.68

Table 3. Horizontal and vertical FWHM intensity of Ti channels

BeamProp Simulations

Having demonstrated low loss waveguides in SLN, we use the measured properties to determine the optimal directional coupler design for the photomask. The measured mode size in Ti:SLN fabricated waveguides was used as feedback into the Beamprop modeling to determine the material parameters in the diffusion model, then these diffused waveguides were used in directional coupler simulations to determine the relationship between waveguide gap and coupling length. This provided us with the waveguide gap and target coupling length used in the final mask design.

Diffusion Model Parameters

We have returned to the diffused waveguide mode field simulations to find a set of material modeling parameters, which when used with the trial fabrication process ($w=6\mu\text{m}$, $\tau=0.0900\mu\text{m}$, $t=22\text{hr}$, $T=1050\text{C}$), yield a mode that matches our observed mode of $3\times 5\mu\text{m}^2$ FWHM beam intensity. The Beamprop simulations yield mode size measurements as FWHM of the electric field strength. The translated size of the measured mode is $4.3\times 7.4\mu\text{m}^2$ FWHM electric field strength.

The model assumes diffusion lengths are proportional to the square root of time, as is typical for a diffusion process, and are given by the Arrhenius form

$$D_i = 2\sqrt{tD_i^0 \exp(-E_i^0/k_B T)} \quad (13)$$

Here t and T are the diffusion time and temperature, respectively, and k_B is Boltzmann's constant. The diffusion model assumes independent diffusion lengths normal and transverse to the surface, thus the subscript in these quantities assumes either value b for the bulk or s for surface diffusion. We find that the experimental mode size ($4.3\times 7.4\mu\text{m}^2$ FWHM electric field strength) is reproduced well by the model when $D_{surf}^0 = 0.0025\mu\text{m}^2/\text{hr}$, $D_{bulk}^0 = 0.0005\mu\text{m}^2/\text{hr}$, and $E_{surf}^0 = E_{bulk}^0 = 2.5\text{eV}$. Figure 17 shows this simulated mode.

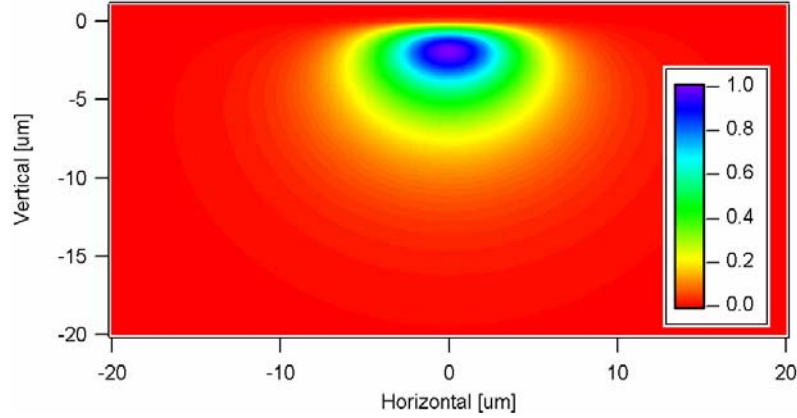


Figure 17. Simulated mode that matches the experimental Ti:SLN mode

Directional Coupler Simulations

The diffusion model parameters determined above were used to simulate the directional coupler to find the optimal gap for fabrication. The effective index method was used, which we have shown to yield excellent coupling length results when compared to a much more computing-intensive 3D beamprop simulation.

The results are shown in Figure 18. We see good agreement with the expected exponential dependence of L_c on waveguide gap. Based on this result, we set the waveguide gap to 9 μm in the mask, which targets a 6 mm coupling length. We allowed for a range of coupling lengths ranging from 3 mm to about 24 mm, as described below.

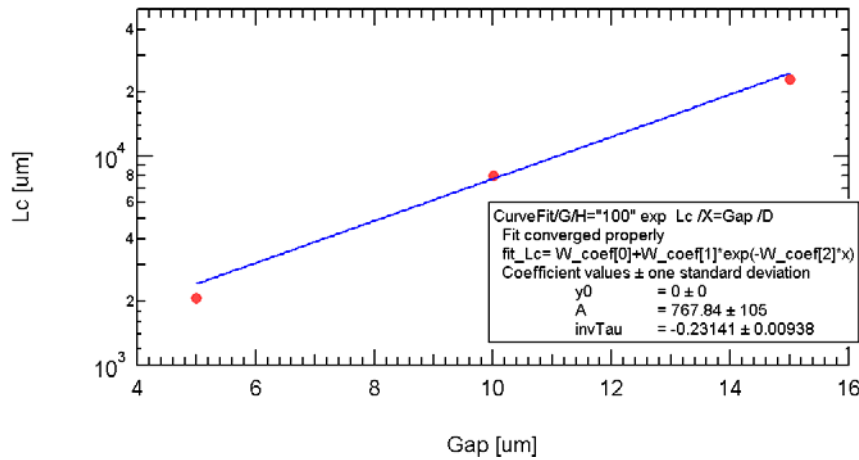


Figure 18. Simulated coupling length dependence on the waveguide gap

Using the same diffusion model, we also looked at the coupling length as a function of the Ti strip width. We find a strong dependence, based on a changing mode size. The uncertainty in the mode size in the fabricated devices due to Ti strip width variations (or otherwise) underscores the importance of providing a variety of devices on the mask with various coupling lengths. The results are shown in Figure 19 below.

The target was $L_c=6400\text{ }\mu\text{m}$, and we see variations in L_c from a low of $4000\text{ }\mu\text{m}$ up to a high of about $16000\text{ }\mu\text{m}$. This is the basis for the coupling length variations used in the SLN mask.

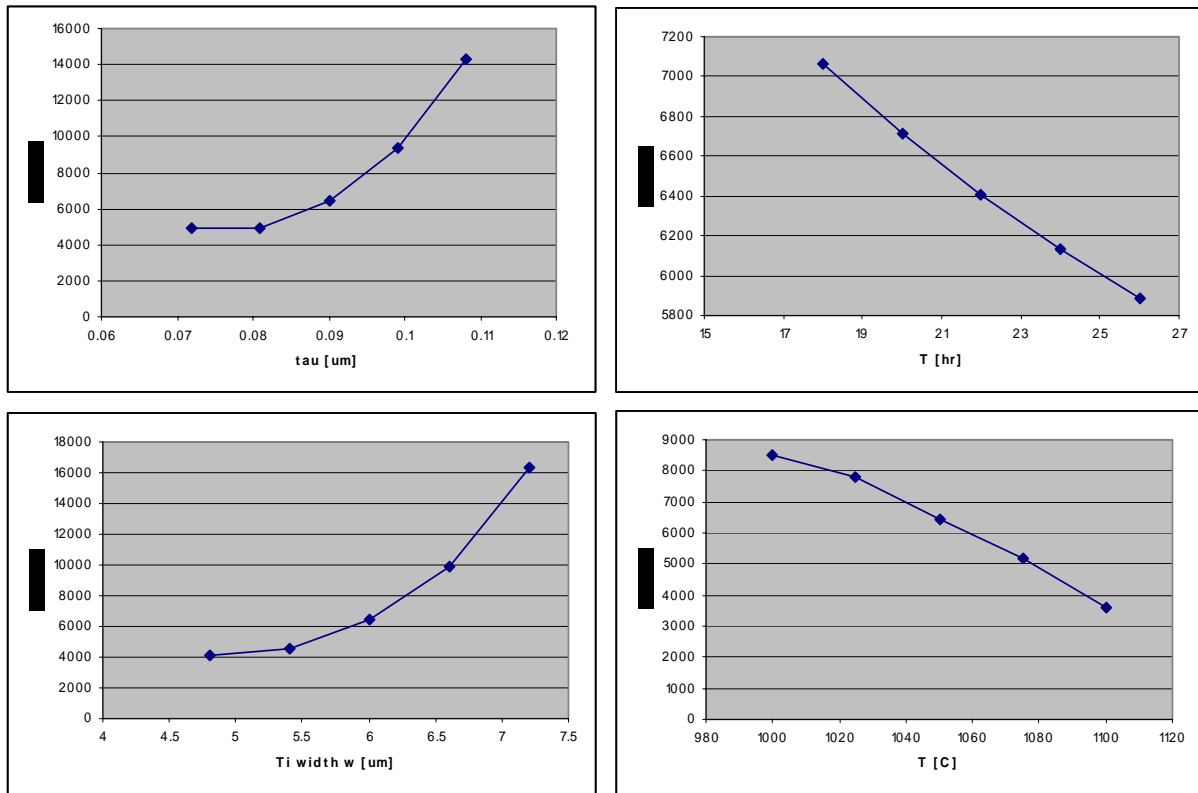


Figure 19. Plots of coupling length vs. various perturbed fabrication parameters

Design of Phase Shifter for the Linearized Coupler

The proton exchange waveguide layer functions as a Ti waveguide overlay that produces phase shifters in the linearized design. The phase shifters work by providing a localized increment in the propagation constant, or equivalently, the effective index, of the waveguide. This section provides a more detailed look at phase shifter operation.

Differential Effective Index

The phase shifter is a waveguide segment of length L that has a proton exchange waveguide overlay on top of the existing Ti diffused waveguide. The differential effective index, Δn_{eff} , is the quantity of interest, because it determines the net phase shift of the phase shift segment:

$$\Delta\phi = L \Delta\beta = kL \Delta n_{eff} \quad (14)$$

where $\Delta\beta$ is the difference in the effective indices between the PE+Ti and the Ti waveguide regions. This section details how this quantity ultimately arises from the additional index change in the waveguide due to the proton exchange overlay.

The proton exchange and Ti diffusion steps each increase the refractive index of the substrate, and the two processes tend to have an additive effect:

$$\Delta n(x, y) \cong \Delta n_{Ti}(x, y) + \Delta n_{PE}(x, y). \quad (15)$$

This means that a small section of Ti waveguide that has proton exchange overlay will have a larger (extraordinary) index delta than the rest of the Ti waveguide. Only the extraordinary index is of interest here since the device is designed for operation using the TM polarized light. While the extraordinary index is increased by the proton exchange overlay, the ordinary index is actually depressed by the proton exchange overlay.

The propagation constant fundamental TM mode, denoted by β , is found by solving for the fundamental mode of the waveguide with index change due to Ti diffusion only. The relationship between the index change and β is as follows:

$$\Delta n_{Ti} \rightarrow \beta \quad (16)$$

Similarly, the waveguide with total index change Δn gives rise to a TM fundamental mode with propagation constant β' :

$$\Delta n \rightarrow \beta'. \quad (17)$$

the incremental propagation constant is given by

$$\beta' = \beta + \Delta\beta \quad (18)$$

This in turn leads to a larger effective propagation constant, and a phase shift of the propagating mode relative to the unmodified Ti waveguide section.

$$n'_{eff} = \frac{\beta'}{k} = \frac{\beta + \Delta\beta}{k} = n_{eff} + \Delta n_{eff} \quad (19)$$

Design Sensitivity

Transfer matrix simulations have shown that the behavior of the linearized design is sensitive to the phase shift imparted by the phase shifters. Due to fabrication uncertainties (namely, the uncertainty in the effective index increment due to the proton exchange layer), fabrication of a phase shifter length based on the ideal design value is unlikely to produce a linearized design. Thus, a good linearized device is assured by designing a number of devices with a range of phase shifter lengths. The phase shifter lengths were chosen based on a target range of Δn_{eff} values ranging from 0.001 to 0.004.

Characterization of the PE Phase Shifter

The aim of the proton exchange process development effort is to produce a fabrication recipe such that the composite proton exchange-over-Ti waveguide layer has a differential effective index Δn_{eff} within the target range. The differential effective index due to proton exchange overlay is characterized using prism coupling in the slab waveguide regions. The effective index deltas that occur in channel waveguides are a close approximation to the measurements made in a slab region.

Proton Exchange on Ti:SLN

The change in the index was characterized for a proton exchange process done on top of Ti diffused SLN wafer. The proton exchange process suppresses the ordinary refractive index. The TE mode, which samples the ordinary refractive index, is not expected to show any waveguiding.

The Ti diffusion process produced four guided modes at 635nm and two guided modes at 1550nm. As expected, the subsequent proton exchange process overlay on the Ti diffused slab eliminated the waveguiding at 1550nm. The initial four modes at 635 nm were reduced to a single guided mode after the PE process. A 2-hour anneal at 350C eliminated guiding at 635nm. No guided modes were observed after continued annealing up to 5 hours.

TM Mode Results at 1550nm

Initial Ti diffusion produced a single guided mode at 1550nm where the index delta for the 0th order mode is 0.015. The PE exchange over Ti:SLN exhibited a single mode behavior, but with slightly decreased 0th mode delta. A 2-hour anneal recovered the 0th mode index delta and still maintained the single mode character. It is still single mode after a 4-hour anneal but the index delta is much reduced. In this case the PE has diffused deep enough that it now is the new “substrate”. After a 5-hour anneal, the measured substrate index partially recovers to the true substrate index value.

Comparisons of the 0th order mode indices of the Ti:SLN and PE+Ti:SLN show that the 2-hour anneal and the 4-hour anneal produce an effective index differential of 0.003 and 0.001, respectively. The mask design for the phase shifters had varying lengths that required a corresponding Ti effective index differential ranging from 0 to 0.004. A 2-hour anneal is expected to produce the desired effective index differential, and a 4-hour anneal would produce too small an index differential. A short phase shifter is made from a large index differential. The ideal phase shifter would have “zero” length.

Proton Exchange on Ti:CLN

A proton exchange process on Ti:CLN followed by a 4-hour anneal produces two TM modes at 1550nm. The second mode is very weakly guided and it is not expected to be a problem to produce suitable phase shifters.

Photomask Design

The photomask is intended to produce a linearized coupler in which the fabricated structures match the theoretical design. In particular, for optimized linearity, it is important the coupler be twice the coupling length, and for the phase shifters to impart the correct phase shift. Uncertainty in the mode size and Ti strip width causes uncertainty in the coupling length. And uncertainty in the index delta created by proton exchange overlay causes an uncertainty in the phase shift created by the phase shifters. We have put a 2D array of devices on the mask such that these two quantities are independently varied. The linearized coupler device is of the Pi-phase shift type.

In addition, the photomask was designed to produce waveguides, Mach-Zehnder, standard directional coupler and Y-coupler modulators and periodic segmented waveguide (PSW) structures.

PSW Structures

We added a number of periodically segmented waveguide input structures to the mask. These were added on straight waveguides, and consisted of period 40 mm, lengths 500 and 1000 mm, and a series of aspect ratios ranging from 0.5 to 0.9 at each length. These structures offer good potential for adiabatically increasing the mode size and thus reducing coupling losses to standard fibers. The structures will be tested by measuring the mode field when the PSW is on the output side of the waveguide.

Mask Summary

The table below gives a detailed summary of the chip design.

Chip Num X	Number of Circuits	Circuit_Notes
1	6	straights, widths 5-10 um
1	1	Y-coupler
1	4	Short MZI, no shifters
1	8	Short MZI, various phase shifter lengths
1	32	LDCM, gap 9 um, coupler lengths 1-8, phase shifter lengths 1, 2
2	6	PSW structures (wg width=7)
2	1	Y-coupler
2	12	2x2DC with various phase shifter lengths
2	32	LDCM, gap 9 um, coupler lengths 1-8, phase shifter lengths 3, 4
3	6	straights, widths 5-10 um
3	1	Y-coupler
3	4	Long MZI, no shifters
3	8	Long MZI, various phase shifter lengths
3	32	LDCM, gap 9 um, coupler lengths 1-8, phase shifter lengths 5, 7
4	6	PSW structures (wg width=7) in APE waveguides
4	1	Y-coupler
4	12	2x2DC with various phase shifter lengths
4	32	LDCM, gap 9 um, coupler lengths 1-8, phase shifter lengths 7, 8
5	6	straights, widths 5-10 um
5	1	Y-coupler
5	4	2x2DC with kappa varying structures
5	8	straights, widths 5-10 um
5	32	LDCM, gaps 7, 11 um, various coupler lengths and shifter lengths

Table 4. Photomask summary

Device Fabrication

Device fabrication requires three levels of photomask operation. The first level defines the pattern for Ti diffusion. The second level defines the pattern for the proton-exchange phase shifter and the third level defines the electrode metal.

The waveguide devices were fabricated in CLN and SLN substrates. Figure 20(a) and (b) show schematic of a Mach-Zehnder Interferometer Modulator (MZI) and a Standard Directional Coupler Modulators (SDCM) and Figure 21 shows the schematic of a Linearized Directional Coupler Modulator (LDCM) device. The MZI and SDCM were fabricated using both the Ti diffusion and the PE processes. The LDCM were first fabricated using titanium diffused waveguide channels. The Phase Shifters in LDCM were then created via Annealed Proton Exchange (APE) process over the Titanium diffused waveguide channels in the coupling region.

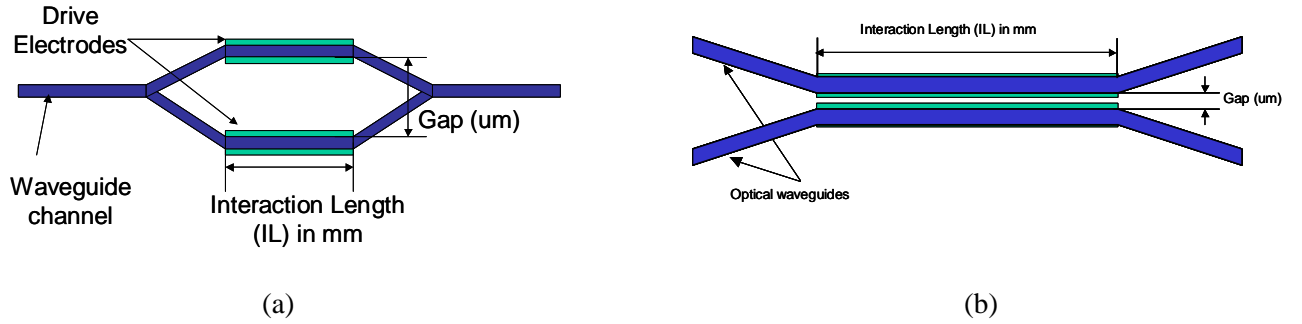


Figure 20. Schematic of MZI and SDCM devices

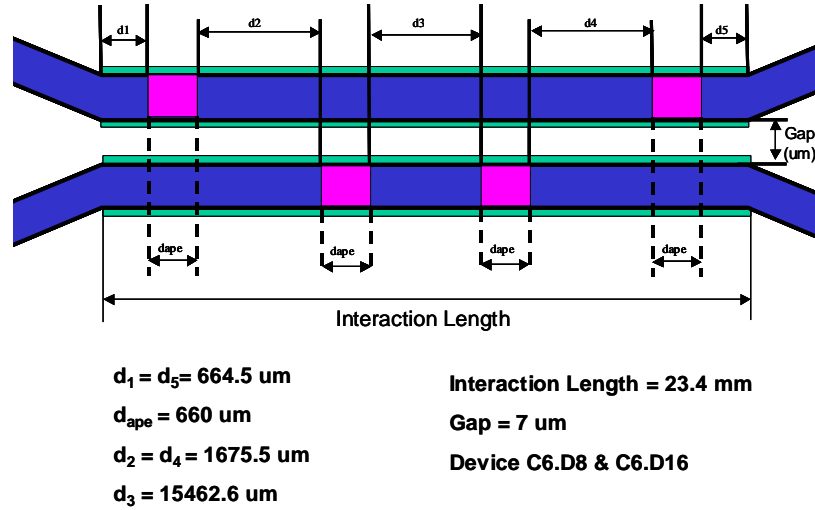


Figure 21. Schematic of a LDCM device

TEST RESULTS

Mach-Zehnder and linearized directional coupler modulators were characterized at audio frequency. Based on these results linearized directional coupler modulator devices were selected for more detailed SFDR measurements. PSW structures were also characterized.

Device Test Results at Audio Frequency

Mach-Zehnder Modulators

The devices were tested at 1550 nm by launching TM mode. The switching voltage V_{π} was observed to be about 7 V-cm for both CLN and SLN based devices. The SLN device has a slightly higher optical loss, about 1 dB, compared to the CLN based device. The extinction ratio, ER, for the both SLN and the CLN device was about 35 dB.

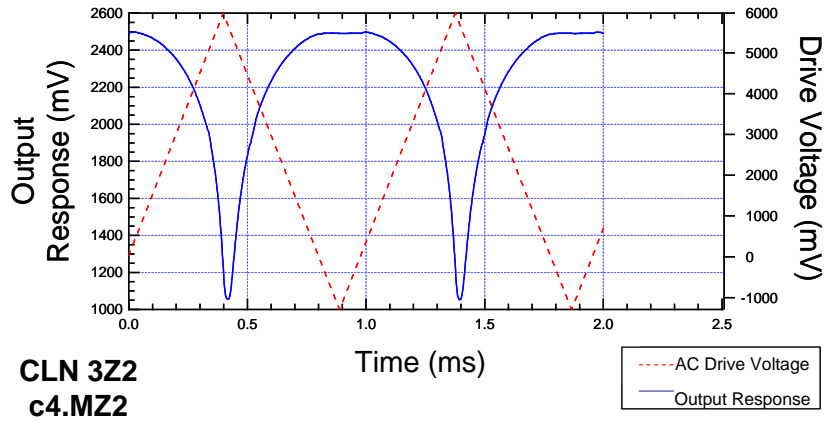


Figure 22. MZI Modulator response for device 3Z2c4.MZ2 fabricated in CLN

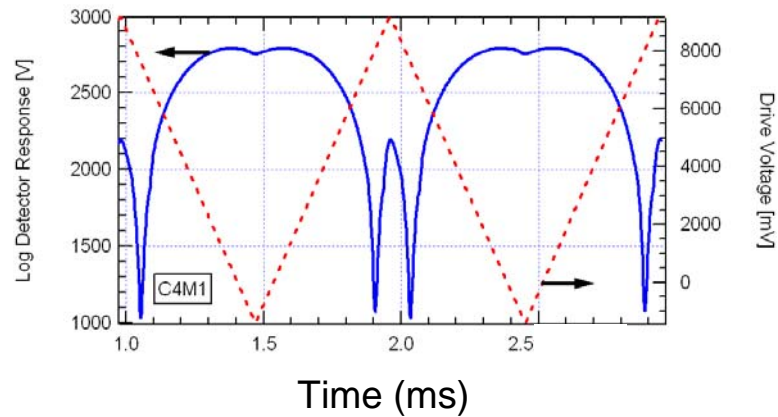


Figure 23. MZI Modulator response for device 2Z2c4.MZ1 fabricated in SLN

Standard Directional Coupler Modulators (SDCM)

Figure 24 and Figure 25 show the response of a SDCM fabricated in a CLN substrate. The switching voltage for this device was found to be about 11Volt-cm. The ER was measured in the cross state to be 26 dB.

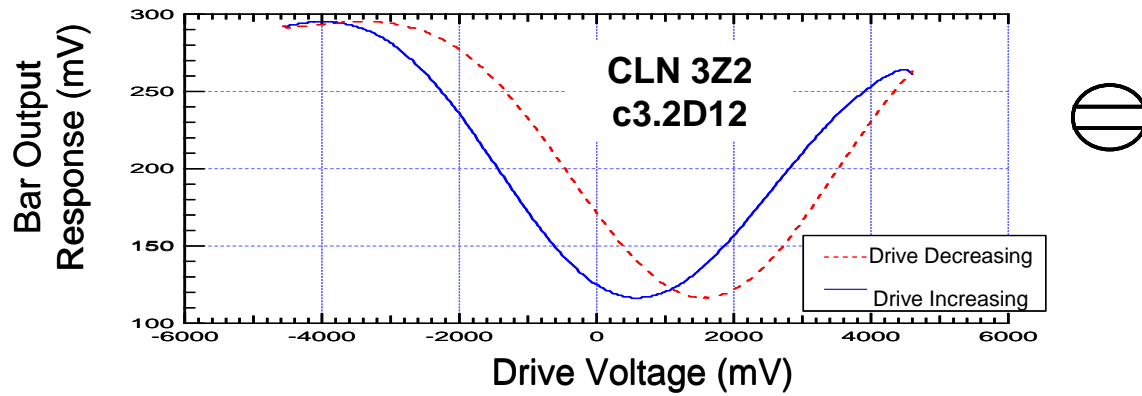


Figure 24. Standard Coupler response in the Bar state

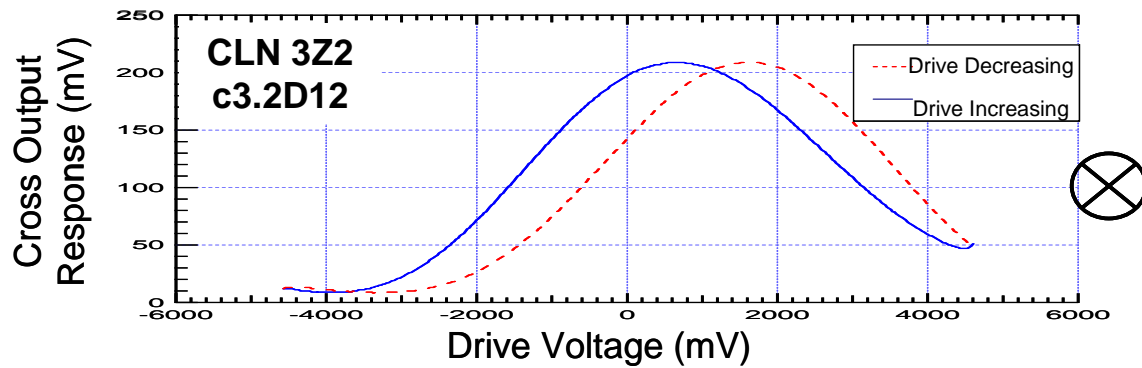


Figure 25. Standard Coupler response in the Cross state

Linearized Directional Coupler Modulators

Figure 26 and Figure 27 show the response of a LDCM device fabricated in a SLN substrate. The switching voltage for this device was found to be 12.4 Volt-cm. The ER was measured in the cross state to be 31 dB.

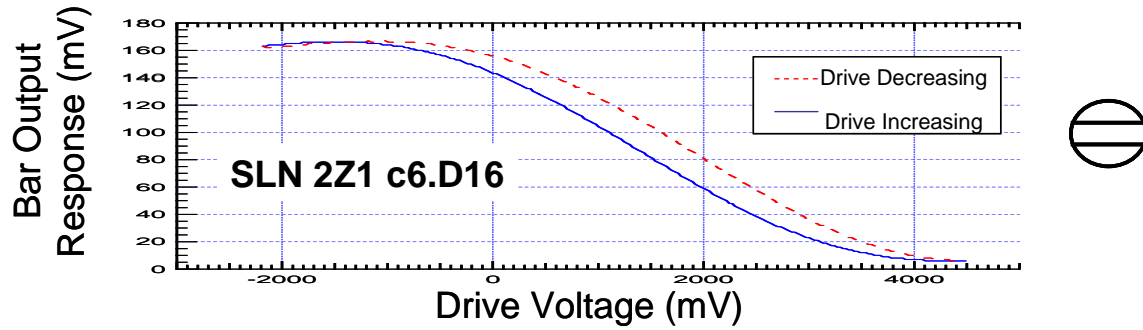


Figure 26. SLN Linearized Coupler response in the Bar state

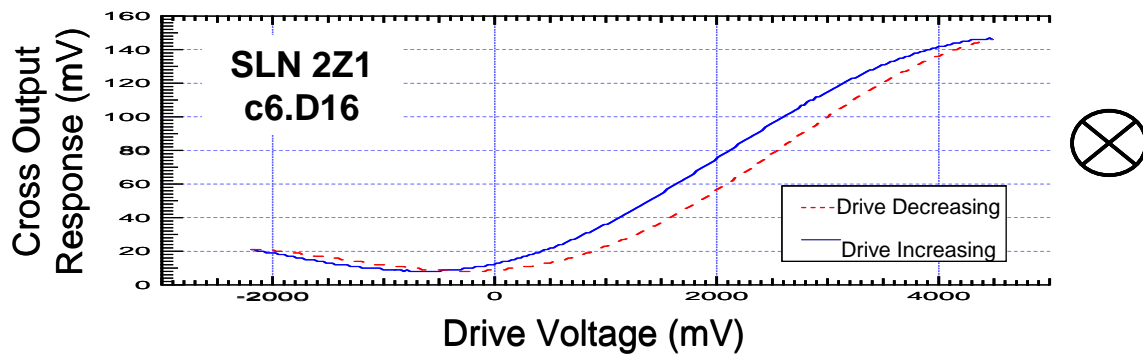


Figure 27. SLN Linearized Coupler response in the Cross state

Figure 28 shows switching characteristics of a LDCM, fabricated in CLN, biased at -1.1 Volt. The switching voltage for this device was found to be 11.7 Volt-cm. The ER was measured in the cross state to be 24 dB. A theoretical cosine-squared MZI transfer characteristic is superimposed on a typical linearized directional coupler transfer characteristic. Qualitatively it can be seen that the transfer characteristic is clearly more linear over a greater range than is the case for the MZI.

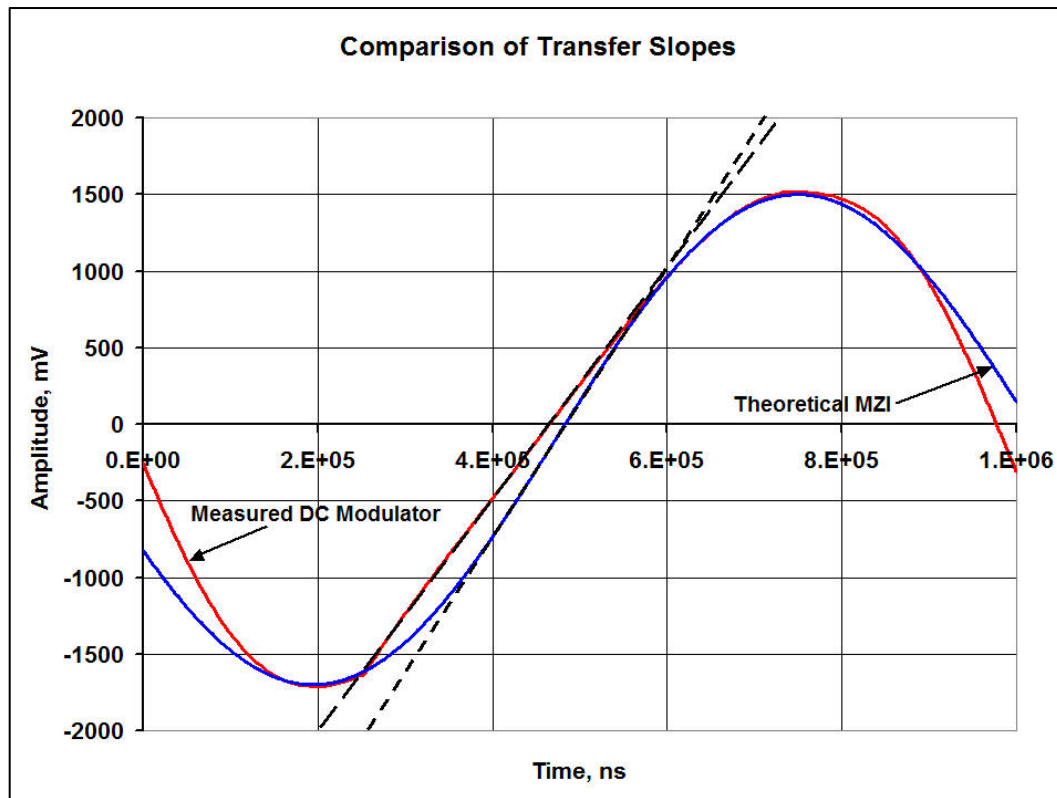


Figure 28. Theoretical MZI response superimposed on a typical LDCM characteristic

PSW Structures

Figure 29 and Figure 30 show a periodic segmented waveguide (PSW) input and output structures, respectively. The waveguides, fabricated in CLN, were tested for TM modes at 1550 nm wavelength. Table 5 and Table 6 summarize the optical transmission loss and mode size for a 7 micron wide waveguide PSW structure (wafer 3Z1). The results show that the PSW structures may be beneficially used to expand the mode size of a lithium niobate waveguide to match that of an optical fiber. To summarize:

- Loss increases when total distance increases because of mode expansion
- Large separation distance also increase loss because of mode expansion
- Shows promise for improved mode matching to fibers

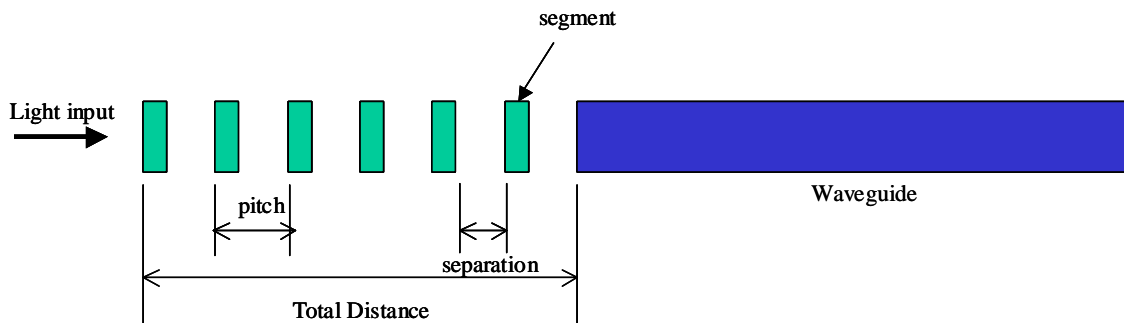


Figure 29. Input PSW structure

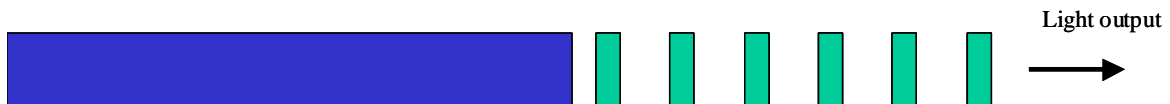


Figure 30. Output PSW structure

3Z1 Summary Table					
Device	Pitch (microns)	length of segment (microns)	separation distance (microns)	Total PSW Distance (microns)	Loss (dB)
Ti7	40	36	4	680	2.76
Ti8	40	28	12	680	2.81
Ti9	40	20	20	680	5.72
Ti10	40	36	4	1680	2.63
Ti11	40	28	12	1680	3.3
Ti12	40	20	20	1680	6.49

Table 5. Optical transmission loss for a PSW structure

3Z1 Summary Table

Device	Pitch/Separation (microns)	Total PSW Distance (microns)	FWHM Horiz x Vert (microns)
Straight Channel Ti			6.25 x 4.98
Ti7	40/4	680	6.47 x 4.93
Ti10	40/4	1680	6.50 x 5.08
Ti8	40/12	680	6.99 x 5.39
Ti11	40/12	1680	7.00 x 5.25
Ti9	40/20	680	8.00 x 5.73
Ti12	40/20	1680	8.55 x 6.77

Table 6. Mode size for a 7 micron PSW waveguide

Spurious Free Dynamic Range (SFDR) Measurements

In this section we detail our measurements on linearized directional coupler modulators whose design is based on the approach detailed earlier. An MZI and two linearized DC devices were tested. These linearized DC devices as identified by their chip reference numbers were LDCM-SR043004.2.3 (3Z2) D16 and LDCM-SR043004.2.6 (3Z2) D16, and the best results are reported below.

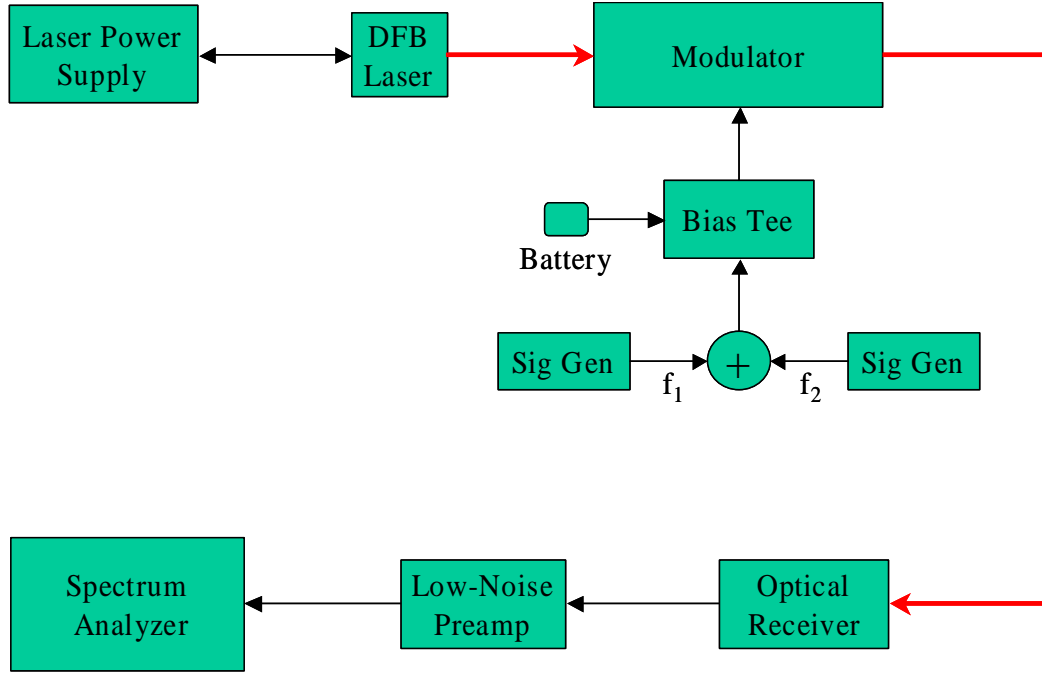


Figure 31. Test system for the measurement of SFDR

Figure 31 shows the test setup for measuring the SFDR. The optical source was a 1550 nm Ortel DFB Laser, model 1710 and controlled by a Laser Power Supply manufactured by ILX. The Optical Receiver was a Dual-Balanced New Focus, model 1617. The saturation power level for this receiver is about +7 dBm. The modulator was inserted between the optical source and optical receiver. The Bias-Tee for the modulator was powered from a 9V battery. The polarity of the bias could be changed using a switch and the manual bias control consisted of a 10-turn potentiometer for providing very fine adjustment. One of signal generators was an Agilent model 33120A Function Generator, while the other was the tracking generator output of a Spectrum Analyzer, model HP 8519E placed in the zero-span mode. Both signal generators produced fairly pure tones with low harmonic content. These two-tone RF signals were summed into the Bias-Tee. Typically, the Agilent signal generator would be set to provide a tone f_1 at 10 MHz and the spectrum analyzer set to provide a tone f_2 at 11 MHz. The Optical Receiver's output was amplified by a 20 dB Low-Noise Amplifier, Sonoma model 330. The intermodulation was observed on a model HP 8583E Spectrum Analyzer.

As mentioned, the chosen frequencies for the RF tones were 10 MHz and 11 MHz. For these frequencies the first, second and third order intermodulation products are given by:

1st-order: f_1, f_2
10 MHz, 11 MHz

2nd-order: $2f_1, 2f_2; f_1 \pm f_2$
20 MHz, 22 MHz; 21 MHz, 1 MHz

3rd-order: $3f_1, 3f_2; 2f_1 \pm f_2, 2f_2 \pm f_1$
30 MHz, 33 MHz; 31 MHz, 9 MHz; 32 MHz, 11 MHz

To measure SFDR at any particular bias, the signal generator's output levels were made equal and adjusted in 1 dBm increments. The HP 8593E was set in Table Mode and markers were placed on representatives of the 1st, 2nd and 3rd-order intermodulation products – these frequencies being 10 MHz, 21 MHz and 31 MHz, respectively. For each value of the selected two-tone RF input level the screen was dumped to a printer in quick succession, and the marker amplitudes subsequently read off the hard-copy plots. SFDR plots were made based on the RF drive levels and these measured amplitudes of the intermodulation products. Data points that showed clear saturation effects or inadequate Signal-to-Noise Ratio (SNR) were discarded and not plotted.

Operation of the New Focus 1617 Receiver

The optical receiver used for the SFDR measurements reported here is Dual-Balanced receiver that can accept complementary inputs. This can provide advantages not only in providing an additional 3 dB of Link Gain but also help in the cancellation of 2nd-order distortion products produced by photodetector themselves, particularly at higher powers. However, for this project this receiver was operated using only one of its inputs, even though the MZI and directional couplers tested had complementary outputs. In the case of the directional couplers tests, this gave us the opportunity to separately access the modulation performance using the Bar and X-Bar outputs. For these directional couplers the X-Bar output was the one used, as these provided the best outputs.

Mach-Zehnder Modulator

Before proceeding with the measurement of the linearized directional coupler, a measurement was done on a standard MZI modulator to establish a baseline, compare with the expected result and to become “comfortable” with the measurement and plotting techniques.

Certain minor corrections were made for RF impedance mismatches and data obviously indicating distortion products from other parts of the system, such as the signal generators, LNA or optical receiver, were not plotted. Generally, there was only a limited range of two-tone RF inputs where satisfactory data could be obtained that was not affected by saturation elsewhere in the system or too little SNR. A typical MZI SFDR plot is shown in Figure 32. The trend line for the fundamental has a slope that is close to 1, while the 3rd-order component is close to 3. The SFDR for the MZI at a mean received optical power of 0 dBm was estimated to be $101 \text{ dB/Hz}^{2/3}$.

Since the received optical power increased by a factor of 10 dB when the power is extrapolated to +10 dBm, the fundamental signal will increased by 20 dB. We can now re-plot the MZI SFDR characteristic given in Figure 32. Figure 33 shows this extrapolated third-order SFDR for the MZI, which has now increased to $111 \text{ dB/Hz}^{2/3}$. This is close to the expected SFDR for a standard MZI in phase-quadrature at a mean received optical power of +10 dBm. This MZI SFDR is used as a benchmark by which the efficacy of other types of modulator can be compared.

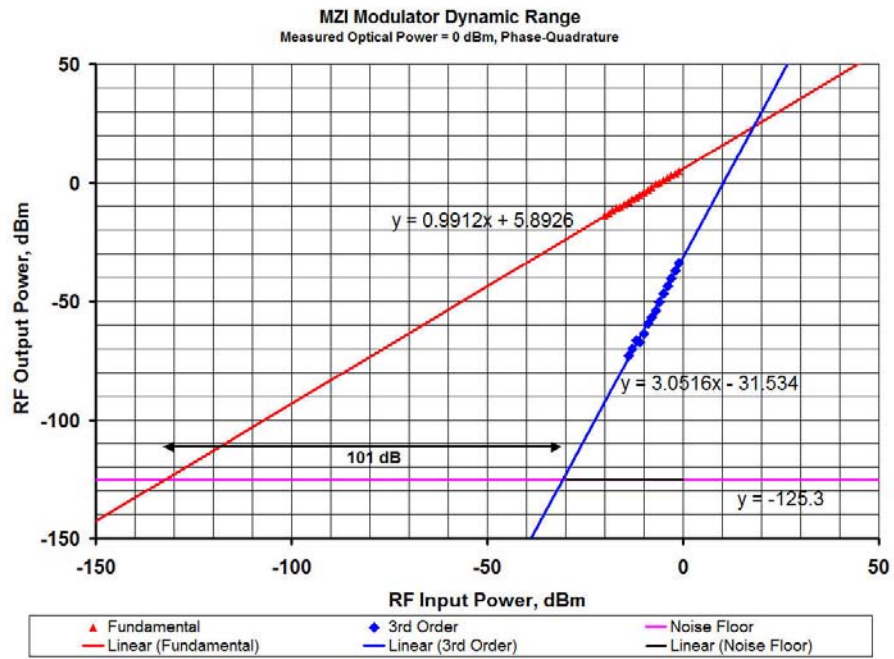


Figure 32. SFDR plot for a MZI modulator for received optical power of 0 dBm

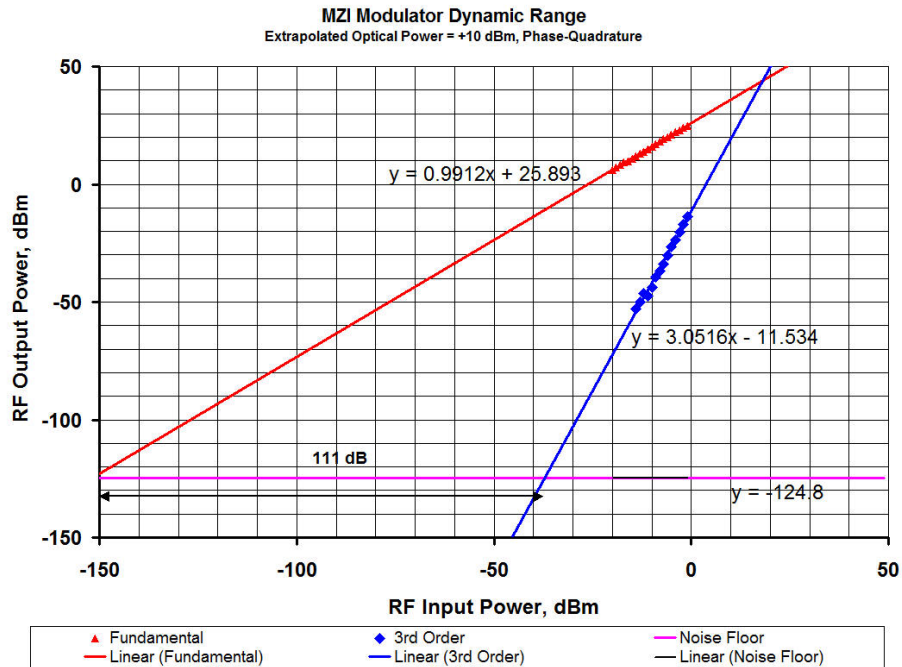


Figure 33. SFDR plot for a MZI for extrapolated mean received optical power of +10 dBm

Linearized Directional Coupler Modulator SFDR Measurements

Before describing the SFDR measurements undertaken on the linearized directional coupler modulators, we will explain in more detail the procedure for extrapolating the measured data from around 0 dBm to a normalized power of +10 dBm.

Extrapolating SFDR Characteristics to Higher Optical Receiver Powers

For comparison purposes, SFDR characteristics are usually normalized to a mean received optical power of +10 dBm, where it is expected that the receiver will be heavily shot-noise limited. The effect of the increase in power on the fundamental signal (and link gain) and the amplitudes of all the intermodulation products is easy to calculate, because it is simply $20 \times$ power ratio by virtue of the action of the square-law photodetector. We assume, of course, that we have an ideal optical receiver that is not generating its own distortion products at the high power. As an example, consider the situation where the (electrical) amplitude of the 1st-order signal is x dBm_e for an optical signal at power 0 dBm_o. To make this clearer and avoid confusion, we have temporarily used the sub “e” and “o” to differentiate between electrical and optical dBm. Then the amplitude of the 1st-order photodetector signal will increase to $0 + 2(10 - x)$ dBm_e when the optical input power is increased to +10 dBm_o. Similarly, the amplitudes of all the recovered harmonics and intermodulation products increase by the same amount.

As previously mentioned, the New Focus 1617 receiver had a saturation power level of about +7 dBm. Optical losses in our system typically limited the received power to be at 0 dBm or less. At these powers, the receiver is kT-noise limited. Thus, to extrapolate the SFDR performance to 10 mW we need to know what the shot-noise limited noise floor will be at +10 dBm – all other things being equal. Figure 34 shows the measured noise floor of the receiver as measured on the HP 8593E spectrum analyzer with the 20 dB Sonoma pre-amplifier, and its extrapolation to a power level of +10 dBm. The noise floor was measured at 15 MHz, which was a “quiet” spot between the 10 MHz and 11 MHz tones and their intermodulation products.

To obtain the characteristic shown in Figure 34, the DFB laser was connected directly to the optical receiver and run at full power, which was about +14 dBm. To change the optical power reaching the receiver, varying levels of optical attenuation were introduced between the patch cords linking the laser to the receiver. The DFB laser source was likely producing about 3 dB of excess intensity noise over the quantum limit.

At 0 dBm the measured kT-limited noise floor is at -128.2 dBm/Hz. At +7 dBm the measured shot-noise floor has risen to -126.3 dBm/Hz. The best-fit curve was extended beyond +10 dBm to obtain the +10 dBm extrapolated noise floor of -124.8 dBm/Hz. This noise floor is used to plot the horizontal receiver noise floor line in the respective extrapolated SFDR plots that will be shown later for the LDC devices.

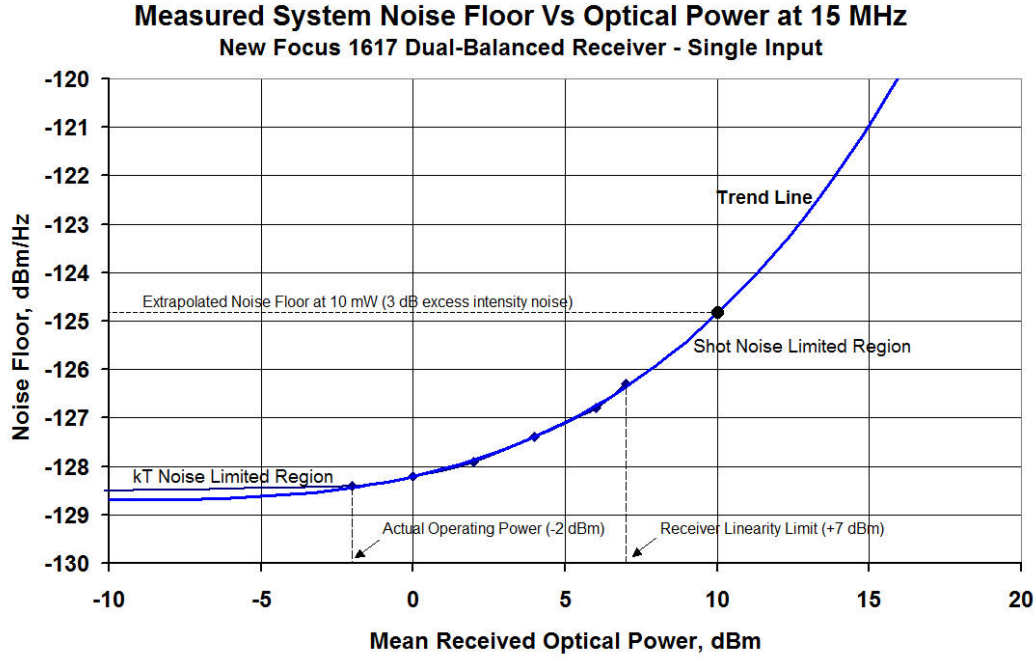


Figure 34. Characterization of New Focus 1617 receiver as a function of mean received optical power

The linearized directional coupler device # LDCM-SR043004.2.6 (3Z2) D16 had a measured $V_{\pi} = 4.6$ V at 1 kHz. The theoretical best bias for standard DC modulator is $0.43 \times V_{\pi}$, which in this case would correspond to +2.0 V. It was found that for the linearized directional coupler device the minimum 2nd-order distortion occurred when the bias was +1.74 V.

Unlike the case of a standard MZI with a cosine² intensity transfer characteristic and deterministic phase-quadrature “sweet-spot” for best linearity, i.e., minimum 2nd-order and maximum 3rd-order, the best place to bias a linearized DC is not immediately obvious. Measurements were taken at several different bias points to obtain some assessment of the devices linearity, under time and effort constraints and the somewhat laborious manual method of measuring SFDR. It is unlikely that measurements were taken at the best bias points, but the data to follow should be representative of device performance.

It was found that the bias point was relatively stable at constant room temperature, so that only minor “tweaks” were needed to maintain the bias at a given point on the transfer characteristic. After selecting a particular bias point, the bias voltage was kept constant while the SFDR data was collected.

Figure 35 shows a typical spectrum of intermodulation components. Markers 1, 2 and 3 measure the amplitudes of the 10.10 MHz fundamental, the 21.10 MHz second-order component and the 31.10 MHz third-order component. Using the procedure described earlier, similar plots were made for different RF levels and the values read off the hard-copy and plotted to produce the SFDR graph.

In SFDR plot is shown in Figure 36. The linear trendline for the fundamental has a slope of 1.0563, the second-order trendline has a slope of 2.0885, and the third-order trendline has a slope of 3.0025. These slopes are very close to 1, 2 and 3, respectively. The 2nd-order SFDR is 79 dB while the 3rd-order is 94 dB for the thermally-noise limited optical receiver at -2 dBm input. The measured thermal noise floor is at a level of -128.5 dB/Hz.

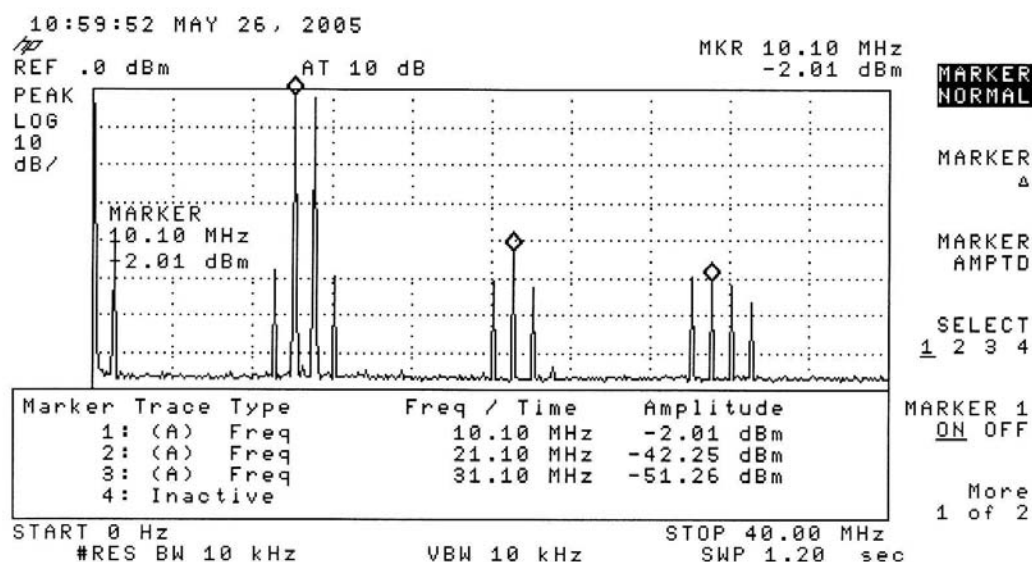


Figure 35. Intermodulation frequency spectrum for LDCM device

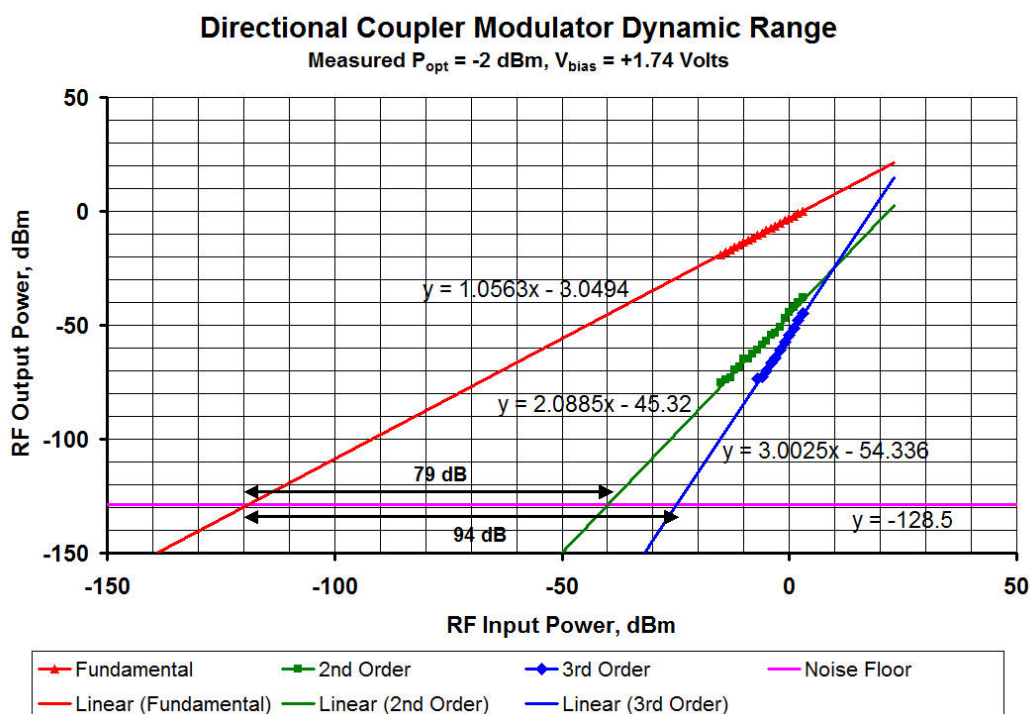


Figure 36. SFDR plot for a bias voltage of +1.74 V and received power of -2 dBm

The plot in Figure 36 under-reports the SFDR because the received optical power is low and the optical receiver is kT noise limited. As was done for the MZI, the SFDR figure was extrapolated to a normalized received power of +10 dBm. This result is shown below in Figure 37.

The SFDR of optical systems is usually compared to a reference power of 10 mW. We can estimate the SFDR performance at +10 dBm rather than at the measured -2 dBm by adding 24 dB to the 1st, 2nd and 3rd-order components, and determining what will be the system noise floor at that power. At a mean received power of -2 dBm the optical receiver is kT noise limited, while at +10 dBm it will be significantly shot noise limited. Again, the plot of optical receiver noise floor as a function of mean received optical power was used to obtain the estimate for the value of the noise floor if the received power had actually been +10 dBm, and if the receiver had been able to handle that amount of optical power without saturation.

As before, the linear trendline for the fundamental has a slope of 1.0563, the second-order trendline has a slope of 2.0885, and the third-order trendline has a slope of 3.0025, and these slopes are very close to the expected 1, 2 and 3, respectively. The 2nd-order extrapolated SFDR is now 88 dB while the 3rd-order is 106 dB for the shot-noise limited optical receiver at +10 dBm input. The thermal noise floor is at a level of -125 dBm/Hz.

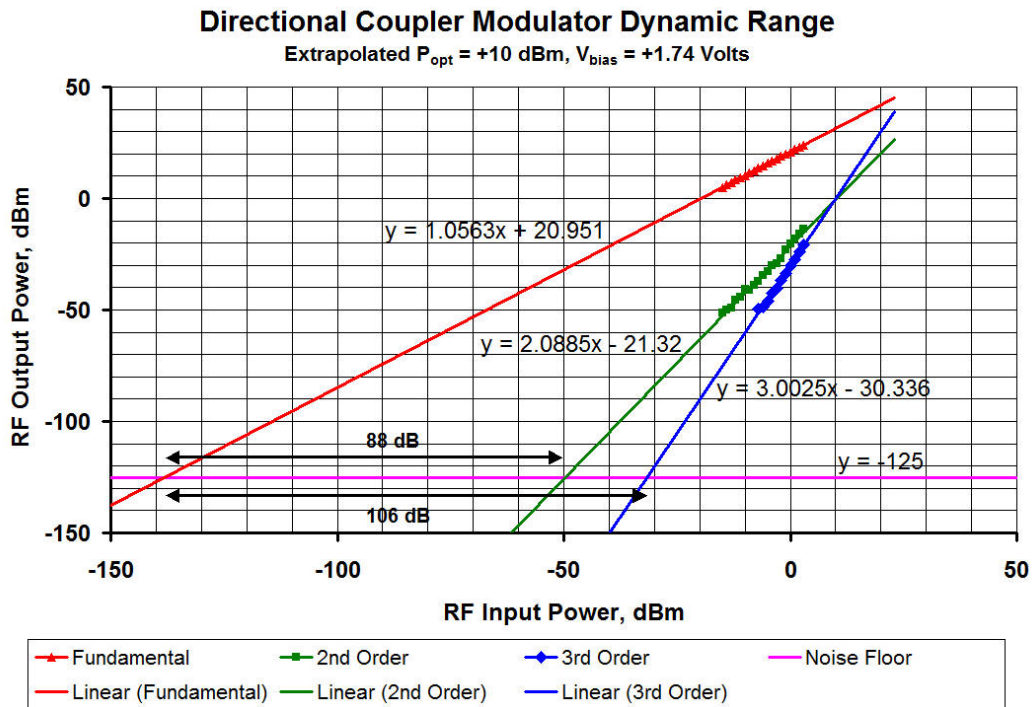


Figure 37. SFDR at a bias voltage of +1.74 V extrapolated to a received power of +10 dBm

Linearized Directional Coupler Modulator Characterization at Different Bias Voltage

A further set of data was collected at a different bias point and this showed improved SFDR results. The bias point was changed from +1.74 V to +1.54 V. The plot of Figure 38 shows the corresponding results.

For this plot the mean received optical power at the +1.54 V bias point was -1 dBm, and the corresponding Link Gain (includes effect of 20 dB Sonoma pre-amplifier) was -1 dB. The linear trendline for the fundamental has a slope of 0.9975, the second-order trendline has a slope of 1.9880, and the third-order trendline has a slope of 2.9991. These slopes are very close to 1, 2 and 3, respectively. The 2nd-order SFDR is 95 dB while the 3rd-order is 102 dB/Hz^{2/3} for the thermally-noise limited optical receiver at -1 dBm input. The thermal noise floor is at a level of -128 dBm/Hz.

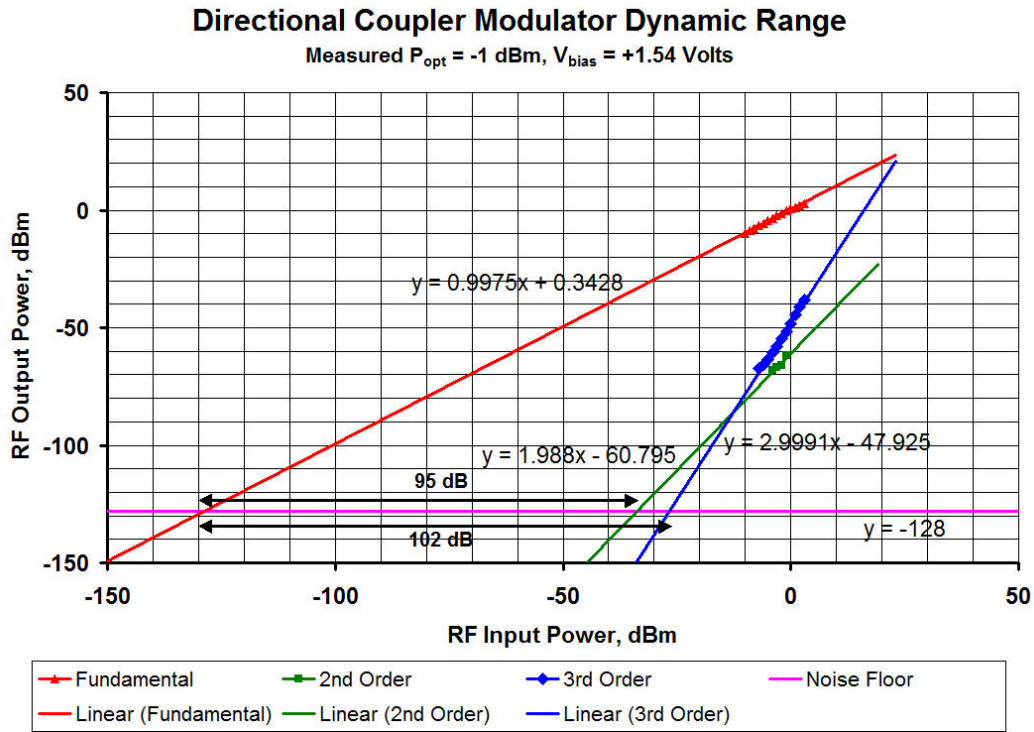


Figure 38. SFDR plot for a bias voltage of +1.54 V and a received power of -1 dBm

The SFDR of optical systems is usually compared to a reference power of 10 mW. We can estimate the SFDR performance at +10 dBm rather than at the measured -1 dBm by adding 22 dB to the 1st, 2nd and 3rd-order components, and determining what will be the system noise floor at that power. At a mean received power of -1 dBm the optical receiver is kT noise limited, while at +10 dBm it will be significantly shot noise limited. The Link Gain at the +1.54 V bias would be +21 dB. Again, this includes the 20 dB gain of the Sonoma pre-amplifier.

For Figure 39, the extrapolated noise floor at +10 dBm will be -124.6 dBm/Hz for the particular DFB laser used as the source. Because of the attenuation produced by a modulator, we would expect most of the excess intensity noise, say 3 dB, to be suppressed at this mean received optical power level. Thus, the quantum noise floor level assumed for the SFDR plot is probably about 3 dB less than this figure, i.e., at -127.6 dBm/Hz.

The SFDR slopes remain the same at 0.9975, 1.9880, and 2.9991, for the 1st, 2nd, and 3rd-order products respectively. The extrapolated to +10 mW 2nd-order SFDR = 104 dB/Hz^{2/3} while the 3rd-order SFDR = 114 dB/Hz^{2/3}.

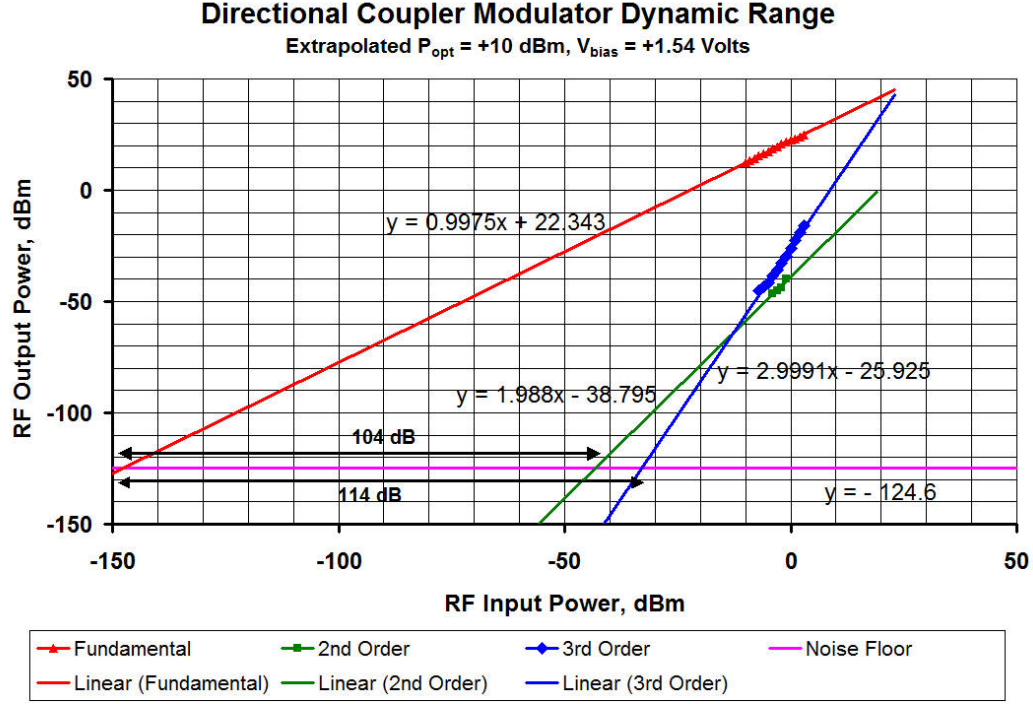


Figure 39. SFDR at a bias voltage of +1.54 V extrapolated to a received power of +10 dBm

Discussion

We have indicated that the measurement of SFDR for these prototype linearized directional couplers is more labor intensive than is the case for the deterministic MZI because without significant investigation of the transfer characteristic it is difficult to know where the “sweet” spot is located. Also, whether 2nd or 3rd-order intermodulation performance is of primary concern will depend on the need for sub-octave operation or operation over the entire baseband. Unlike the case for the MZI with its single deterministic “sweet” spot, there are several points, as was shown earlier, on the linearized directional coupler transfer response where the even or odd intermodulation products are minimized. Matters are further complicated by the characteristic of the linearized directional coupler where, when the 2nd-harmonic is minimized, the higher-order even intermodulation products are not simultaneously minimized.

Because of limitations on the power available at the optical receiver, SFDR measurement values had to be extrapolated to the usual normalized received optical power of +10 dBm. This introduces some uncertainty as to the true level of the system noise floor, and hence the extrapolated SFDR value though it does help mitigate the distortion products from the optical receiver and pre-amplifier as these devices are not driven so hard. That said, it appears possible to obtain a 3rd-order SFDR of similar magnitude to that of the standard MZI. Indeed, these very preliminary results appear to indicate the possibility of squeezing out a few extra dB of dynamic range, which, if it needs to be repeated here, is the object of DC

linearization. The best result for the 3rd-order SFDR appears to be about 114 dB/Hz^{2/3} for +10 dBm at the receiver and negligible RIN impairment.

We would recommend that for linearized directional coupler SFDR measurements, a more automated technique be developed to both step through the transfer characteristic while measuring the amplitudes of the significant low-order intermodulation products. One cannot use the theoretical best bias point based on the “ideal” device, because the prototype devices in particular will differ significantly from so-called “ideal” devices as the effect of fabrication tolerances will not be fully understood during the early work, and as usual, there are always bias drift effects that have to be accounted for.

REFERENCES

- ¹ M. L. Farwell, Z. Lin, E. Wooton, and W. S. Chang, “An Electro-optic Intensity Modulator with Improved Linearity,” *IEEE Phot. Tech. Lett.*, **3**, 792-795, 1991.
- ² C. H. Bulmer, and W. K. Burns, “Linear Interferometric Modulators in Ti:LiNbO₃,” *J. Lightwave Tech.*, **LT-2**, 512-521, 1984.
- ³ T. Li, C. Laliew, and A. Gopinath, “An Iterative Transfer Matrix Inverse Scattering Technique for the Synthesis of Co-directional Optical Couplers and Filters,” *IEEE J. Quantum Elec*, **35**, 375-379, 2002.
- ⁴ C. Laliew, S. W. Lovseth, X. Zhang, and A. Gopinath, “A Linearized Optical Directional-Coupler Modulator at 1.3μm,” *J. Lightwave Tech.*, **18**, 1244-1249, 2000.
- ⁵ G.-H. Song, S.Y. Shin, “Design of corrugated waveguide filters by the Gel’fand-Levitan-Marchenko inverse scattering method,” *J. Opt. Soc. Am. A*, vol. 2, pp. 1905-1915, 1985.
- ⁶ E. Peral, J. Capmany, J. Marti, “Iterative solution to the Gel’fand-Levitan-Marchenko coupled equations and application to synthesis of fiber gratings,” *J. Quantum Electron.*, vol. 32, pp. 2078-2084, December 1996.
- ⁷ T. Tamir, Editor, *Guided Wave Optoelectronics*, Springer-Verlag, Second edition, 1988.
- ⁸ K. Winick, “Design of corrugated waveguide filters by Fourier transform techniques,” *IEEE J. Quantum. Electronics*, vol. 26, pp. 1919-1929, 1990.
- ⁹ S.W. Lovseth, “Optical directional couplers using the linear electro-optic effect for use as modulators and filters,” Dipl. Engineer thesis, Physics, Department, Norwegian University of Science and Technology, May 20, 1996 (project performed in the University of Minnesota 1995-96).
- ¹⁰ S. W. Lovseth, C. Laliew, A. Gopinath, “Amplitude response of optical directional coupler modulator by The Fourier transform technique,” *Proceeding of the 8th European Conference on Integrated Optics*, pp. 230-233, April 1997.
- ¹¹ S.W. Lovseth, C. Laliew, A. Gopinath, “Synthesis of amplitude response of optical directional coupler modulators,” 1997 IEEE-MTT-S International Microwave Symposium digest, vol III, pp. 1717-1720, June 1997.
- ¹² Anand Gopinath, Chanin Laliew, Sigurd Lovseth, Synthesis of optical modulator response IEEE International Topical Meeting on Microwave-Photonics Technical Digest, paper MC-4, pp. 41-43, 12-14 October 1998, Princeton, NJ.(Invited Talk).
- ¹³ Chanin Laliew, Xiaobo , Zhang, A. Gopinath, “Linearized optical directional modulator,” *Integrated Photonics Research Meeting*, July 1999, Santa Barbara, CA.
- ¹⁴ Laliew, X. Zhang, A. Gopinath, “Linearized optical directional-coupler modulators for analog RF/Microwave transmission systems,” *IEEE MTT-S International Microwave Symposium*, pp. 1829-1832.
- ¹⁵ C. Laliew, K.H. Baek, A. Gopinath, “A synthesized electrooptic directional-coupler modulator at 1.3 microns with low switching voltage,” 2002 Conference on Lasers and Electro-Optics Technical Digest, paper CMI2, pp. 42, 2002, O.S.A.
- ¹⁶ K. H. Baek, C. Laliew, A. Gopinath, “The wavelength dependence of a synthesized electro-optic co-directional coupler modulator with phase shifters,” 2002 Integrated photonics Research Meeting Technical Digest, paper IThD3-1, Vancouver, BC, 2002, O.S.A.
- ¹⁷ Oxide Corp., www.opt-oxide.com.
- ¹⁸ Y. Furukawa, K. Kitamura, S. Takekawa, A. Alexandrovski, R. K. Route, M. M. Fejer, and G. Foulon, “Improved material properties in MgO-doped near-stoichiometric LiNbO₃ for nonlinear optical applications,” *IEEE Conference on Lasers and Electro Optics (CLEO-2000) Technical Digest*, 386-387, San Francisco, USA, 2000.

- ¹⁹ F. Agullo-Lopez and J. Garcia Sole, "Point Defects in LiNbO₃," *Properties of Lithium Niobate*, K. K. Wong, Ed., 15-22, INSPEC, IEE, London, United Kingdom, 2002.
- ²⁰ M. Yuki, T. Oka, H. Yamauchi, H. Nakajima, S. Kurimura and K. Kitamura, "Ti Diffused Optical Waveguides in Stoichiometric LiNbO₃," Technical Report of Institute of Electronics Information Communication Engineers, OPE 2001-111, 2001.
- ²¹ H. Nakajima, M. Yuki, T. Oka, H. Yamauchi, S. Kurimura, I. Sakaguchi, and K. Kitamura, "Ti-diffused waveguides fabricated on stoichiometric LiNbO₃," *Photonics in Switching (PS-2002)*, Cheju, Korea, 242-244, 2002.
- ²² F. Caccavale, D. Callejo, C. Dragoni, A. Morbiato, M. Musolino, F. Cavuoti, M. Dellagiovanna, F. Lucchi, V. Pruneri, P. Galinetto, D. Grando, and C. Sada, "Identification of LiNbO₃ compositions with optimized functional properties for advanced electro-optical devices," paper presented at SPIE Photonics West 2004, San Jose California, USA, January 2004.
- ²³ E. Strake, G. P. Bava, and I. Montrosset, "Guided Modes of Ti:LiNbO₃ Channel Waveguides: A Novel Quasi-Analytical Technique in Comparison with the Scalar Finite-Element Method," *J. Lightwave Tech.*, Vol. 6, pp. 1126-1135, 1988.